2009

Pseudo-monoenergetic x-ray diffraction measurements using balanced filters for coherent-scatter computed tomography

Stephen R. Beath
Western University

Pseudo-monoenergetic x-ray diffraction measurements using balanced filters for coherent-scatter computed tomography

(Spine title: Pseudo-monoenergetic x-ray diffraction measurements)
(Thesis format: Integrated article)

by

Stephen R. Beath

Faculty of Medicine and Dentistry
Department of Medical Biophysics

2

Submitted in partial fulfillment
of the requirements for the degree of
Master of Science

School of Graduate and Postdoctoral Studies
The University of Western Ontario
London, Ontario, Canada

March 9, 2009

THE UNIVERSITY OF WESTERN ONTARIO
SCHOOL OF GRADUATE AND POSTDOCTORAL STUDIES

CERTIFICATE OF EXAMINATION

Chief Advisor

Dr. Ian A. Cunningham

Advisory Committee

Dr. David Holdsworth

Dr. Deidre L. Batchelar

Dr. Jerry Battista

Examining Board

Dr. Grace Parraga

Dr. Eugene Wong

Dr. Martin King

The thesis by

Stephen R. Beath

entitled

Pseudo-monoenergetic x-ray diffraction measurements using balanced filters for coherent-scatter computed tomography

is accepted in partial fulfillment of the
requirements for the degree of
Master of Science

Chair of Examination Board

Dated this 9th day of March, 2009.

Abstract

In the treatment of kidney stones, knowing stone composition has been established as an important aid to the understanding of stone formation and in preventing recurrences, particularly the composition of the initial "core" of the stone. Traditionally, stone composition has come from laboratory techniques such as infrared spectroscopy and x-ray diffraction. These methods require taking multiple samples of excised stone fragments and powdering them - losing structural information in the process, and therefore the specific core composition.

Coherent-scatter computed tomography (CSCT) is a method of non-destructive "composition" imaging based on measurements of diffraction patterns from tissues. Use of an x-ray tube degrades scatter-pattern angular resolution due to the x-ray spectral width, making it difficult to uniquely identify some materials. The use of two transmission filters with similar atomic numbers (balanced "Ross filters") to generate pseudo-monoenergetic scatter patterns of common kidney stone components is described as it applies to CSCT. We show that an analysis of angular-blur mechanisms reveals that focal spot size and beam width are the most important factors determining Bragg-peak width when erbium and thulium balanced filters are used. A Bragg-peak RMS angular width of approximately 0.14° (relative width of 3% at 5° scatter angle) can be achieved, reducing peak-overlap in the scatter functions of common kidney stone constituents.

CSCT is capable of producing 3-D material-distribution maps. In previous studies, such maps were of relative material density. We describe a theoretical method to generate absolute (g/cm^3) mass-density distributions.

Balanced-filter CSCT improves scatter-function angular resolution and allows for the measurement of common kidney-stone constituents with non-overlapping peaks.

Key words: coherent scatter, x-ray diffraction, x-ray scattering, computed tomography, composition imaging, kidney stones, renal calculi, balanced filters, Ross filters

Co-Authorship

The following thesis contains material from manuscripts either accepted or submitted for publication.

Chapter 2 has been accepted by Medical Physics as "Pseudo-monoenergetic x-ray diffraction measurements using balanced filters for coherent-scatter computed tomography" by S. R. Beath and I. A. Cunningham. I developed the theory, designed, performed and interpreted the experiments, and wrote the manuscript under the supervision of I. A. Cunningham.

Chapter 3: I implemented the balanced-filter method on the prototype CSCT system in our laboratory with the assistance of Dr. S. Lazarev, including electronic hardware design, construction and software control. I designed, performed and interpreted the experiments and wrote the manuscript under the supervision of I. A. Cunningham.

Contents

List of Tables

List of Figures

List of Acronyms & Abbreviations

3-D	Three-dimensional
Al	Aluminium
BF	Balanced filter
CCD	Charge-coupled devices
COD	Calcium oxalate dihydrate
COM	Calcium oxalate monohydrate
CP	Calcium phosphate
CPD	Calcium phosphate dihydrate
CS	Coherent scatter
CSCT	Coherent scatter computed tomography
CsI	Cesium iodide
CT	Computed tomography
Cu	Copper
CYS	Cystine
Er	Erbium
ESWL	Extracorporeal shock wave lithotripsy
Gd	Gadolinium
IRS	Infrared spectroscopy
keV	Kiloelectron volt
kVp	Peak kilovoltage
mA	Milliamperes

MAP	Magnesium ammonium phosphate hexahydrate
mAs	Milliampere-second
MHU	Mega-heat unit
NEQ	Noise-equivalent number of quanta
NNLS	Non-negative least squares
PC	Personal computer
PMMA	Polymethyl methacrylate
RMS	Root mean square
SNR	Signal-to-noise ratio
Tm	Thulium
UA	Uric acid
x	Momentum transfer argument
XRD	X-ray diffraction
μCT	Micro computed tomography
ζ	Fraction of scattered photons that contribute to a particular Bragg peak

Chapter 1

Introduction

1.1 Urinary stone disease

Approximately one in 10 North Americans will develop kidney stones during their lifetime.[1] Of these, approximately 75% will recur without follow-up treatment.[2] The resulting renal stone disease, if left untreated, can cause severe morbidity. For example, stasis of the urine can lead to renal infection that may go on to cause permanent kidney damage.[3] Mortality, too, is a risk, particularly in elderly populations where complications arising from stone disease such as hypertension or acute renal failure can have life-threatening consequences.[4] To make matters worse, over the past 25 years kidney stone incidence rates have increased,[5] a trend that is expected to continue.[6]

Successful treatment of kidney stones involves both the immediate removal of an obstructing calculus and a long-term strategy, such as lifestyle or dietary changes, to prevent stone recurrence.[7]

Extracorporeal shock wave lithotripsy (ESWL) has emerged as the primary mode of kidney stone therapy. ESWL pulverizes stones into small fragments that may pass unobstructed through the urinary tract. Unfortunately, treatment success rates with ESWL have stalled at 75%.[8] It has been suggested that because certain types of

kidney stones are known to be impervious to ESWL, and because stone composition currently cannot be determined prior to treatment with existing imaging modalities, failures may result in the unnecessary use of ESWL in cases where it is known to not be effective.[9]

Measures taken to prevent stone recurrence can involve lifestyle changes or pharmaceutical intervention.[7] The treatment pathway is determined by the composition of the stones as determined by laboratory analysis of calculi which have been removed from the body or passed after ESWL.

Both ESWL and recurrence prevention strategies benefit from knowledge of stone composition. Yet in the case of ESWL, no extracorporeal imaging technique exists that can adequately determine the composition of a kidney stone within the body.[10] Similarly, a recent study has shown that conventional laboratory analysis techniques of excised stones can result in misleading estimates of bulk composition.[11]

The focus of this thesis is to develop the use of an imaging technique, known as coherent-scatter imaging, that will allow for adequate determination of kidney stone composition *ex vivo* today and open the door to *in situ* imaging in the future.

1.1.1 Etiology

Kidney stones are hard crystal masses of minerals or proteins that form in the presence of urine.[12] They can be found anywhere within the urinary tract.[13] Sizes range from as small as a grain of sand to golfball sized and beyond. Calculi with diameters less than 5mm are usually able to pass through the urinary tract[14], but larger diameters can cause blockages which require medical intervention.[15]

The supersaturation of urine with minerals and other chemicals is responsible for initial crystal formation and subsequent growth.[12] Urine mineral imbalances are linked to a number of risk factors, including nutrition,[16] obesity,[17] genetics, metabolic and physiological abnormalities, and socioeconomic status.[18]

Urinary stones are 98% crystalline,[19] with mineral crystals deposited onto an

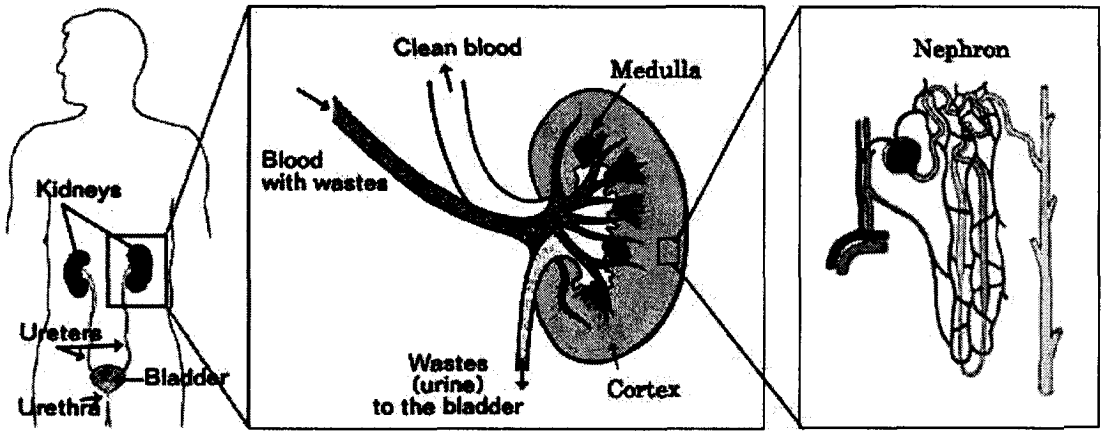

Fig. 1.1: Schematic illustrating functional structures of the urinary system, modified from the National Kidney and Urologic Diseases Information Clearinghouse

organic matrix. Over 50 types of components have been recognized. The vast majority of all stones are made of the seven materials listed in Table 1.1. Of these, stones that are composed of calcium compounds (oxalate and phosphate), uric acid, ammonium phosphate, and cystine, are the most common.

1.1.2 Treatment of acute renal colic

For the past 25 years, extracorporeal shock wave lithotripsy has been the primary interventional procedure used in the treatment of urinary calculi.[20] Because the majority of kidney stones are acoustically dense, they will absorb a large proportion of the energy in sound waves traveling through the body. An ESWL machine generates high-energy pressure waves outside the body, which are then applied to the surface of the skin and focused on the kidney stone. This results in the kidney stone experiencing severe compressive forces that in many cases will cause it to fracture, allowing the resulting fragments to pass freely through the urinary tract.[21]

Historically, ESWL has a success rate of 75%, with most of the fragmentation failures coming from certain mineral types not amenable to fragmentation.[22, 23]

Component	Abbreviation	Occurrence (%)	Causes
Calcium oxalate monohydrate	COM	43 - 83	Excess oxalate-rich foods (spinach, chocolate), digestive disorders, genetic enzymatic deficiencies
Calcium oxalate dihydrate	COD	55 - 61	Excess dietary calcium, salt or protein. Reabsorption deficiencies in the kidney, hormonal disequilibrium
Calcium phosphate	CP	28 - 61	Alkaline urine, urinary tract infections, hyperparathyroidism, renal malformations
Calcium phosphate dihydrate	CPD	0.5 - 3.2	Acidic urine
Magnesium ammonium phosphate	MAP	9 - 16	Infection by urease-producing bacteria
Uric acid	UA	9 - 20	High urine acidity / small urine volume
Cystine	CYS	0.3 - 1.3	Cystinuria genetic defect

Table 1.1: Summary of common kidney stone mineral components and possible factors in their occurrence.[18] Occurrence rates do not sum to 100% as most stones have multiple components. Chemically "hard" stones which are not amenable to ESWL include calcium oxalate monohydrate, calcium phosphate dihydrate, and cystine. Calcium oxalate dihydrate and magnesium ammonium phosphate stones are considered "soft", with MAP having a sticky consistency that is also particularly difficult to fragment with ESWL.

Should ESWL be unsuitable for use, such as when a stone is located just outside the kidney in the ureter, or should ESWL be ineffective (for example, with non-fragile stones such as cystine), there are surgical options. Percutaneous nephrolithotomy is a procedure where a small incision in the patient's back is made and into which a nephroscope is inserted to remove the stone. Ureteroscopy involves a scope inserted through the urethra into the ureter, after which the physician can remove the stone, or use shock waves or laser pulses to fragment the stone for passage.[7]

One of the main drawbacks of ESWL is that the likelihood of successful stone fragmentation is not assessed before the procedure is performed.[8] Therefore a cohort of patients is being subjected to ESWL even if the technique is known to be ineffective for fragmenting their stone type. For example, stones composed of chemically "hard" minerals such as cystine are difficult to fragment with ESWL.[24] This causes an unnecessary risk to the patients, such as significant renal trauma, for patients with these stone types. This risk could be mitigated if stone composition was known prior to ESWL treatment.

Once the stone or fragments are removed the composition of the material can be analyzed to determine the cause of formation. Since 75% of stones recur without proper medical management, understanding the underlying cause of formation is essential to effective therapy.[2] When a materials analysis is complete, the physician can then recommend measures to prevent recurrence. This could involve increasing fluid intake, recommending that the patient lose weight, limiting dietary protein, sodium, fat and sugar, or other pharmaceutical care.

1.1.3 Stone composition analysis techniques

Material analysis of kidney stones *in situ* is generally not possible at present, although researchers are investigating a number of imaging modalities for this task. Spiral computed tomography proved capable of identify some of the major stone types *in vitro*,[25] but has yet to be proven *in vivo*. Partial volume (due to slice thickness),

scatter and beam hardening effects cause variations in measured Hounsfield(HU) values.[26] With few exceptions, HU values alone are not sufficient to identify urinary calculi. Dual-energy CT has been shown to differentiate certain types of stones better than HU based measurements *in situ*, for example uric acid and calcium-based, but more study is needed on a wider variety of stone types.[27]

In an *in vivo* study of conventional radiography, stone composition was misidentified 61% of the time.[28] Dawson *et al.*, using magnetic resonance imaging, were able to distinguish only a few types of calculi using a T1-weighted sequence.[29]

Once a stone has passed or is surgically removed, several analysis techniques can be used to analyze stone material and structure. These include infrared spectroscopy (IRS), powdered x-ray diffractometry (XRD), polarization microscopy, scanning and transmission electron microscopy, wet chemistry analysis, and Raman spectroscopy.[30]

Today, the most routinely performed *ex situ* laboratory analysis techniques are XRD using Cu Kα x-ray emissions (8 keV) and IRS.[22] However, these are fundamentally surface-analysis techniques, necessitating that each stone be crushed to a powder for analysis.[31] This destructive process results in the loss of knowledge of the structure of the stone. Furthermore, only a small subsample (of order micrograms) is actually interrogated during testing, which may not be representative of the entire stone. For example, the stone mineral magnesium ammonium phosphate is often caused by infection. Thus it may be medically useful to identify if MAP is present at the 'core' of a stone, or the periphery.[22] If it is the core, then a treatment to prevent recurrence should target infection. If it is the outer layers of the stone that contain MAP, the infection may be secondary to the stone itself, and of less concern. Likewise, the microscopy and chemical-analysis based methods can only be used on small isolated stone fragments that may not be representative of the core. *There is currently no practical laboratory analysis technique to provide this information.*

Coherent-scatter computed tomography (CSCT) is a novel imaging technique that *can* provide this information. It has the ability to map both the composition

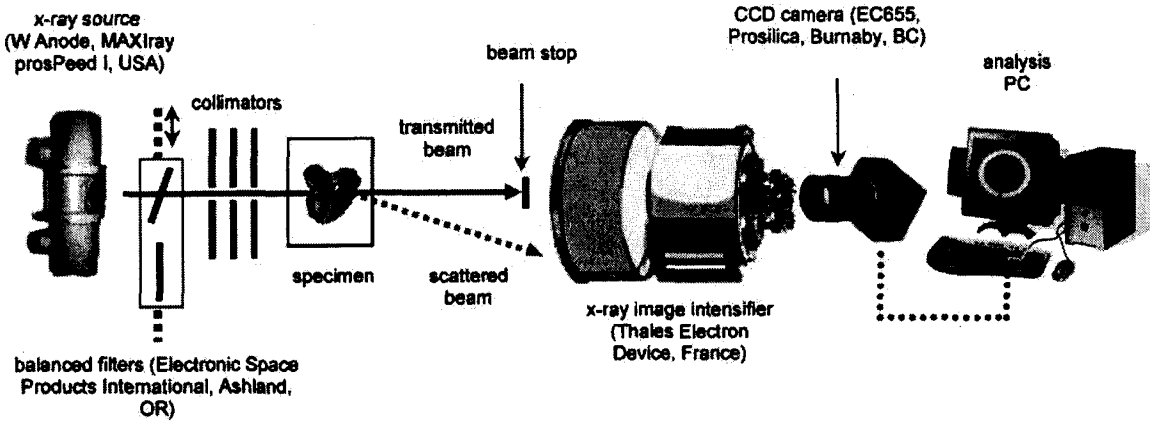

Fig. 1.2: Schematic diagram of the CSCT system.

and structure of small objects non-destructively. The technique combines the material analysis capability of conventional XRD with the non-destructive cross-sectional imaging capability of CT.

1.2 Coherent-scatter based compositional analysis of kidney stones

Our group has developed a coherent-scatter computed tomography system utilizing a diagnostic x-ray tube capable of imaging kidney-stone specimens, as illustrated in Fig. 1.2.[32, 33] Unlike conventional radiographic techniques where image contrast comes from the total attenuation differences among the materials being imaged, CSCT image contrast is determined by the differences in the diffraction pattern of x rays coherently scattered by the material under interrogation.

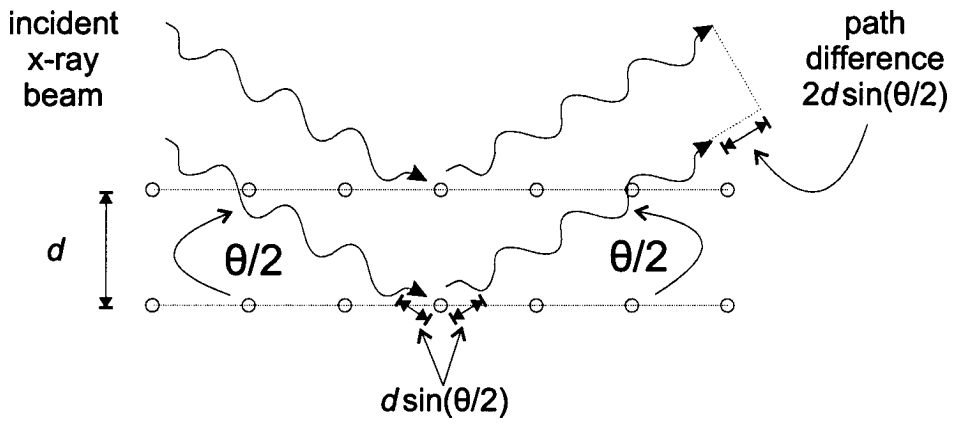

Fig. 1.3: The Bragg relationship. When the path difference of the scattered x rays is an integer multiple of the x-ray wavelength, constructive interference occurs, giving rise to a scatter peak.

1.2.1 Coherent scatter and diffraction of x rays

The theoretical basis of coherent-scatter imaging has been described in detail elsewhere [34, 32] and only a brief summary is given here. The differential coherent-scatter cross section per unit solid angle Ω, per electron, evaluated at scatter angle θ and x-ray energy E, is given by:[35, 36]

$$\left.\frac{\mathrm{d}\sigma_e}{\mathrm{d}\Omega}\right|_{E,\theta} = \frac{r_e^2}{2}(1+\cos^2\theta)\left[|F(\chi)|^2 + F_{KN}(E,\theta)S(\chi)\right], \tag{1.1}$$

in which $(r_e^2/2)(1+\cos^2\theta)$ represents the Thomson scatter cross section for unpolarized x rays where all atomic electrons act as scattering centres, $F(\chi)$ is the coherent-scatter form factor describing interference effects responsible for the scatter patterns measured in this study, $S(\chi)$ is the incoherent (Compton) scatter function, and $F_{KN}(E,\theta)$ is the Klein-Nishina factor. In this equation, χ is termed the momentum transfer argument ($\Delta p = 2h\chi$) and is given by $\chi = (1/\lambda)\sin(\theta/2) = (E/hc)\sin(\theta/2)$.[37] It describes interference effects in the scattered photons (specific to any material) that give rise to characteristic x-ray diffraction patterns.[38]

During coherent interactions, the electromagnetic wave of the incident photons sets the atomic electrons of the scattering material oscillating. These electrons then

emit photons of the same energy as the incident radiation, a form of elastic scattering leaving no energy deposited in the scattering matter.[35] b Diffraction peaks are the result of the interactions between the x-ray electromagnetic wave and bound atomic electrons.[39] Laue posited that regularly-spaced arrays of atoms might form a three-dimensional diffraction grating for x rays.[40] Bragg[41] extended this work and derived the following: diffraction at angle θ (relative to an incident beam) of x rays having wavelength λ from crystal planes with spacings d is governed by the following relationship,

$$n\lambda = 2d\sin(\theta/2), \tag{1.2}$$

known as Bragg's Law. Simply stated, the total path difference for x rays reflected by successive plains must be an integer multiple of the x-ray wavelength for constructive interference to occur.[35] Only first-order diffraction ($n = 1$) is considered here. The resulting scatter patterns are a superposition of peaks corresponding to diffracted photons from each crystal plane. Furthermore, if the diffraction planes are of multiple orientations, such as in powdered or amorphous materials, the resulting scatter peaks will be circularly symmetric about the incident beam.

At diagnostic x-ray energies (30-140keV) coherent scatter interactions account for up to 10% photon interactions.[42] However, coherent scatter is strongly forward peaked ($< 10°$) and dominates over all incoherent scatter at these low angles. This is shown in Fig. 1.4 where values of $|F(\chi)|^2$ (estimated using the independent free-atom model[36, 43]) and $F_{KN}(E,\theta)S(\chi)$ (describing the relative intensities of coherent and incoherent scatter respectively) are illustrated for CaC_2O_4 as a function of scatter angle θ at an energy of 40 keV. Fluorescent photons from photoelectric interactions do not contribute substantially to the scatter signal due to the low atomic number of the absorber and the isotropic direction of the emissions.

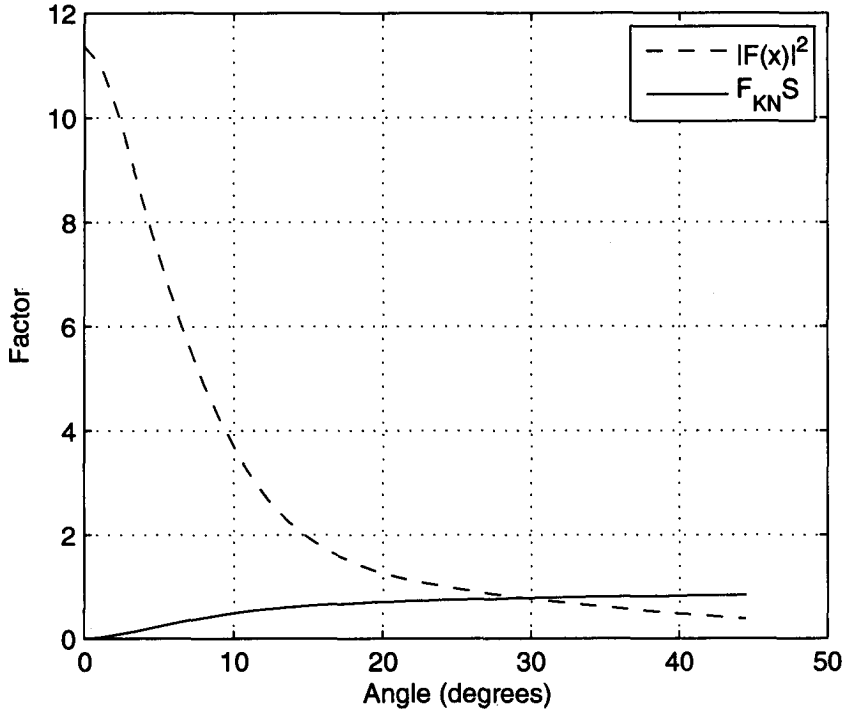

Fig. 1.4: Illustration of the intensity ratio of coherent scatter (using the independent free-atom model) to incoherent scatter (Compton scatter), given by the ratio $|F(\chi)|^2$ to $F_{KN}(E,\theta)S(\chi)$, for CaC_2O_4 as a function of scatter angle at 40 keV.

1.2.2 Coherent-scatter patterns and scatter functions

Figure 1.5 shows examples of coherent-scatter patterns formed by powdered samples of the seven most common kidney stone constituents. The CSCT analysis software integrates this scatter-pattern signal in concentric rings about the scatter centre and normalizes by the ring solid angle to form a material-specific scatter function.

Scatter functions for the same seven kidney stone constituents are shown in Fig. 1.6. Note that each peak in the scatter function corresponds to one or more crystal planes in the mineral. Utilizing a theoretically ideal imaging system, each peak would be a single delta function or combination of delta functions having negligible angular width. As can be seen in several of these examples, whereas the XRD scatter function is composed of discrete peaks, in the CSCT scatter functions some of the discrete peaks are blurred into single wide peaks. This occurs, for example, in the first scatter-function peak of magnesium ammonium phosphate hexahydrate.

Previously, Kozanetsky *et al.* [45] measured a variety of materials' coherent-scatter scatter functions, while Evans *et al.* [46] examined scatter distributions of various types of breast tissues. Speller and Horrocks [47] studied coherent-scatter measurements of tissues of medical interest such as bones and gall stones.

Johns and LeClair [42, 48, 49] modeled both contrast and SNR of bulk coherent-scatter measurements in comparison to traditional attenuation-based radiography over several studies. Recently Johns *et al.* [37] looked at the feasibility of measuring accurate coherent x-ray form factors of amorphous materials using powder diffractometers, and LeClair *et al.* [50, 51] have modeled the potential of coherent-scatter imaging in mammography.

1.2.3 Coherent-scatter computed tomography

The use of coherent-scatter to produce tomographic images was pioneered by Harding *et al.* [34], who adapted crystallographic techniques to a first-generation

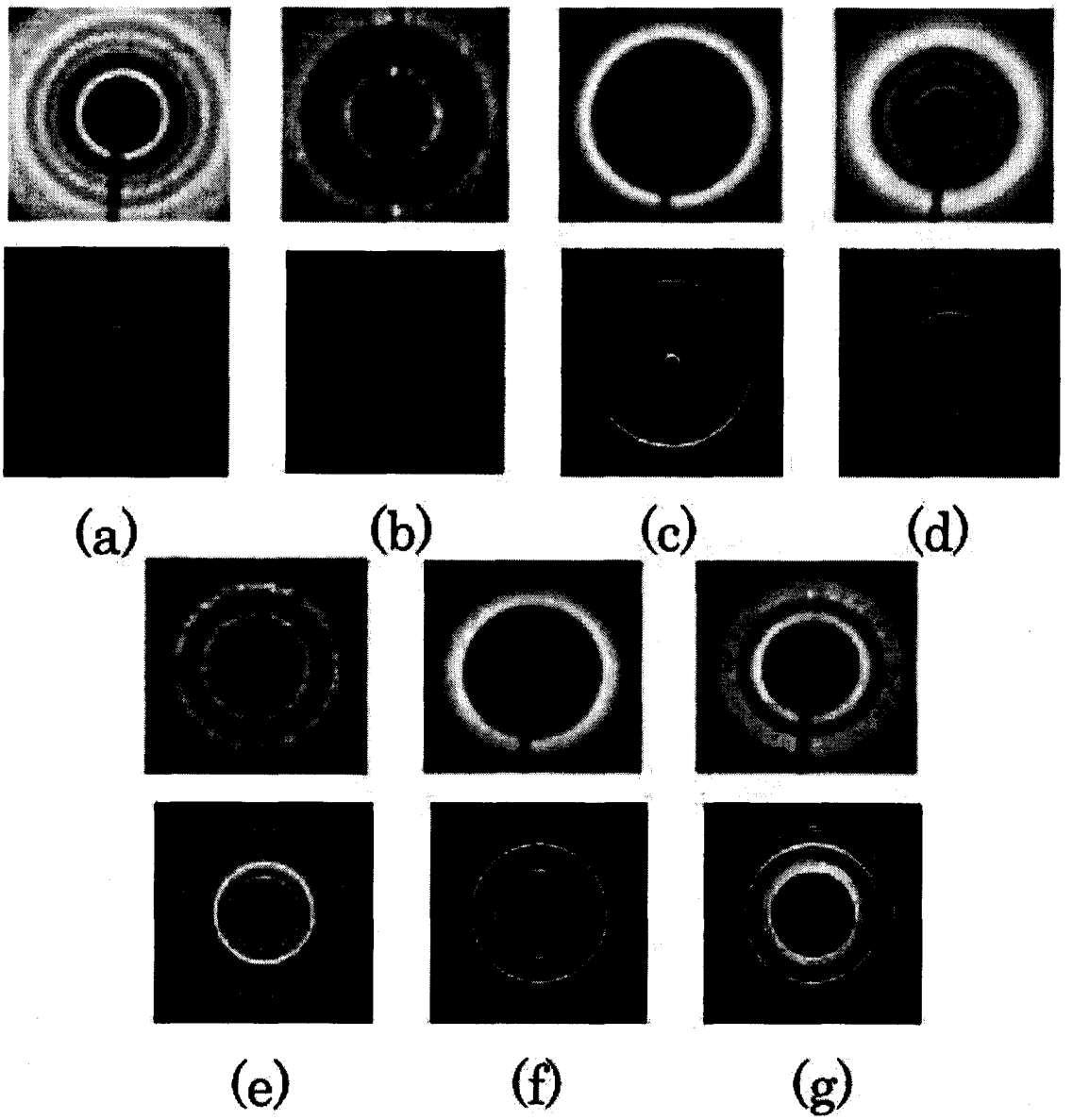

Fig. 1.5: Sample scatter patterns for the seven most common kidney stone constituents (a) calcium oxalate monohydrate, (b) calcium oxalate dihydrate, (c) calcium phosphate, (d) calcium phosphate dihydrate, (e) magnesium ammonium phosphate hexahydrate,(f) uric acid, (g) cystine. Top: patterns were acquired by a Gd-filtered (polyenergetic) CSCT system, bottom: patterns acquired by a Cu k-alpha (monoenergetic) x-ray diffractometer. From *Davidson et al.*[44]

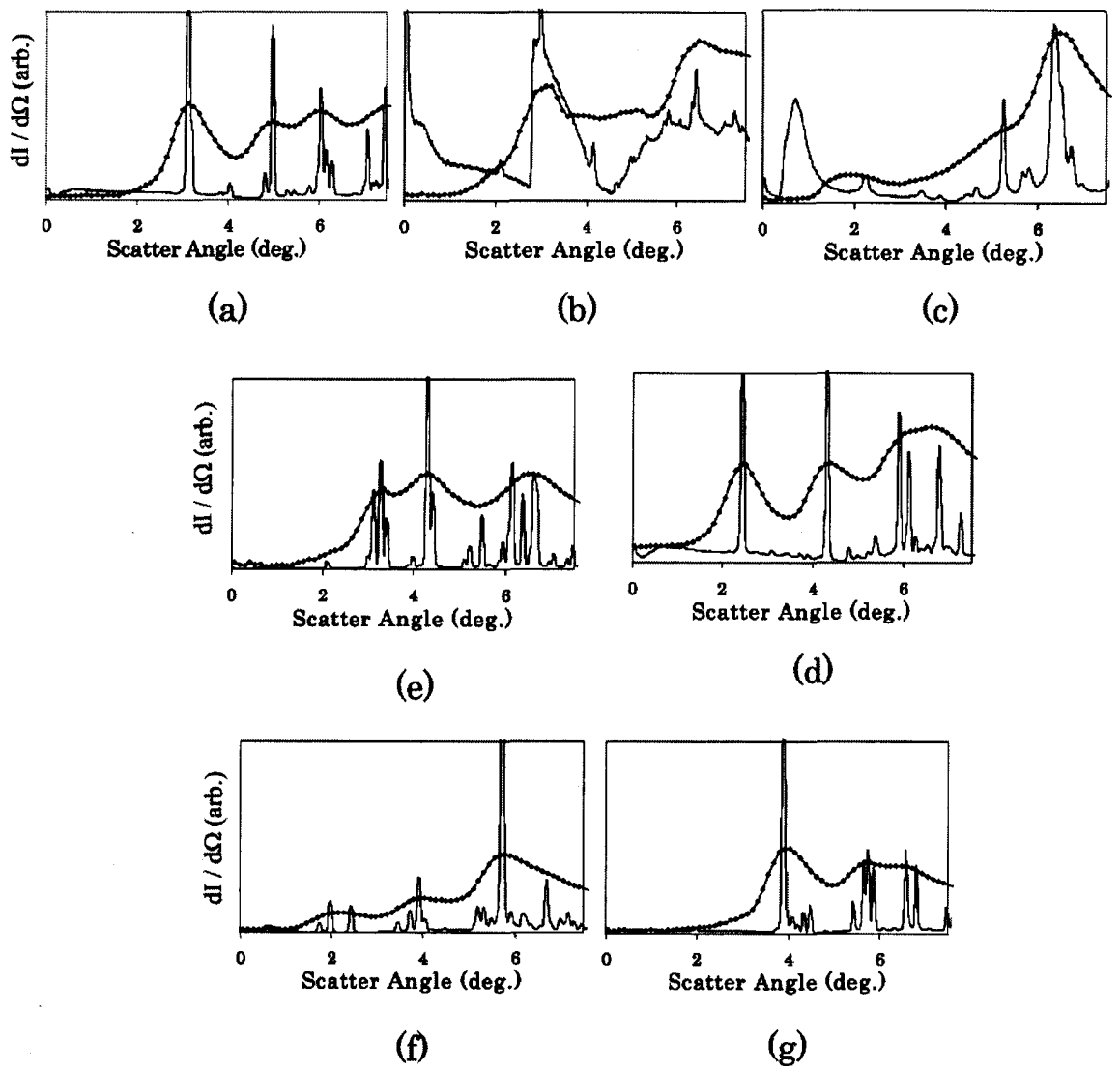

Fig. 1.6: Measured scatter functions from the seven most common kidney stone constituents (a) calcium oxalate monohydrate, (b) calcium oxalate dihydrate, (c) calcium phosphate, (d) calcium phosphate dihydrate, (e) magnesium ammonium phosphate hexahydrate, (f) uric acid, (g) cystine. Darker dotted lines: patterns were acquired by a Gd-filtered (polyenergetic) CSCT system, lighter solid lines: patterns acquired by a Cu k-alpha (monoenergetic) x-ray diffractometer. From *Davidson et al.*[44]

CT arrangement using a diagnostic x-ray tube. Since CT is a transmission-based technique, x-ray sources capable of producing higher-energy photons which will not be completely absorbed by the specimen are required. Harding's system used an array of scintillation detectors to produce angle-specific tomographic slices of an AAPM plastic phantom. Unlike conventional CT which produces a single distribution of x-ray attenuation values across a specimen, Harding showed distributions of scatter at a number of discrete scatter angles.

Westmore *et al.* [52] refined the technique by using an area x-ray image intensifier to capture all of the low-angle scatter emanating from the specimen. A material-identification capability was also added, matching measured scatter functions to a reference library of scatter functions of pure materials. This allowed for the production of relative mass-density distributions of materials within a specimen.

1.2.4 Composition analysis

Different forms of coherent-scatter compositional imaging have been used for non-invasive baggage inspection[53] and food safety certification,[54] as well as a variety of medical detection tasks. Recently, medical CSCT research has been concentrated in two areas: bone density measurement and kidney stone analysis. Investigators such as Kerr *et al.* [55] looked at using both coherent and Compton scatter to determine skeletal mineral status, whereas Royle and Speller [56] proposed measuring coherent-scatter functions to distinguish between healthy and osteoporotic bones. Batchelar *et al.* [57] showed that CSCT is capable of determining the collagen-mineral ratio of intact bone specimens, a capability lacking in existing bone analysis techniques.

The potential of CS to lend insight into kidney stone disease was first investigated by Dawson *et al.* [58], who showed that CS patterns were capable of distinguishing calcium oxalate stones other stone types *in vitro*. Bachelar *et al.* [33] measured coherent-scatter scatter functions for seven of the most common kidney stone constituents. Davidson *et al.* [59] extended this work by demonstrating tomographic

material-specific maps of excised kidney stone specimens, as well as proving that the azimuthal angular dependence of crystalline materials, such as in the scatter function of calcium oxalate dihydrate in Fig. 1.5, is averaged out in a tomographic acquisition.[60] This showed that the accurate detection of crystalline materials was possible.

Recently, Davidson *et al.* [11] demonstrated that the current stone analysis standard, infrared spectroscopy, missed detecting certain types and quantities of stone components that were able to be identified by a CSCT system. With further improvements in instrumentation and additional comparative studies to established techniques, CSCT has the potential to provide compositional information beyond existing modalities in some fields.

A drawback of the CSCT system used in these previous studies is the inability to identify minerals that are not included in the library of reference materials. This is due to CSCT's modest angular resolution (as compared to XRD), which sometimes causes the unique scatter peaks of materials under interrogation to overlap. This peak overlap makes it difficult to ascertain whether an observed peak is a superposition of materials in the reference library or a new, unknown, constituent. Clearly, reducing the angular blur of measured scatter functions would reduce peak overlap.

1.2.5 Factors affecting scatter-function blur

Westmore *et al.* [32] investigated several factors that could affect the angular blurring of scatter functions. These include the effect of object size, x-ray beam width, pixel width and spectral width. An example geometric blur consideration, specimen size, is illustrated in Figure 1.7. Westmore achieved a spectral RMS width of 14% RMS by filtering the polyenergetic tungsten-anode x-ray spectrum with a gadolinium filter. Although the angular resolution obtained with the system was sufficient to resolve unique scatter functions for the majority of materials studied, the scatter-function peaks are spread such that they overlap with each other. This overlap

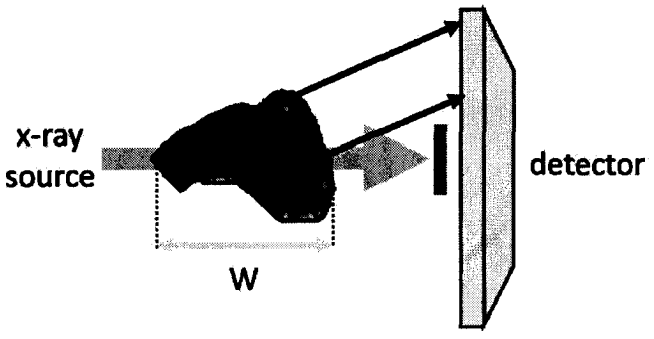

Fig. 1.7: Example of a geometric blur consideration. Scattered photons generated at the front of a specimen will impinge the detector at a different location than photons scattered at the back of the specimen. If the material at the front and back of the specimen is the same (i.e. Bragg peaks occur at the same angles) the sample width W will cause the measured Bragg peak to be broadened on the detector. Note: dimensions exaggerated to illustrate blur effect.

resulted in some inaccuracies: for example, the system misidentified polyethylene as nylon in a scan of an AAPM soft-tissue mimicking phantom.

Westmore's results indicate that the spectral width of the x-ray source dominates all other sources of angular blur. Therefore imaging with a monoenergetic x-ray beam should reduce scatter-peak overlap more than any other blur consideration.

1.2.6 Potential sources of monoenergetic x rays

A number of x-ray sources may be candidates for providing the narrow spectral width required for reducing angular blur in coherent-scatter CT.

Radioisotopes

Radioisotopes are elements with unstable nuclei that undergo radioactive decay to reach a more stable form.[61] Upon decay these elements emit high-energy particles and gamma rays, which are used extensively in both medical imaging and nuclear medicine. The photons produced in radioisotope decay have specific decay energies

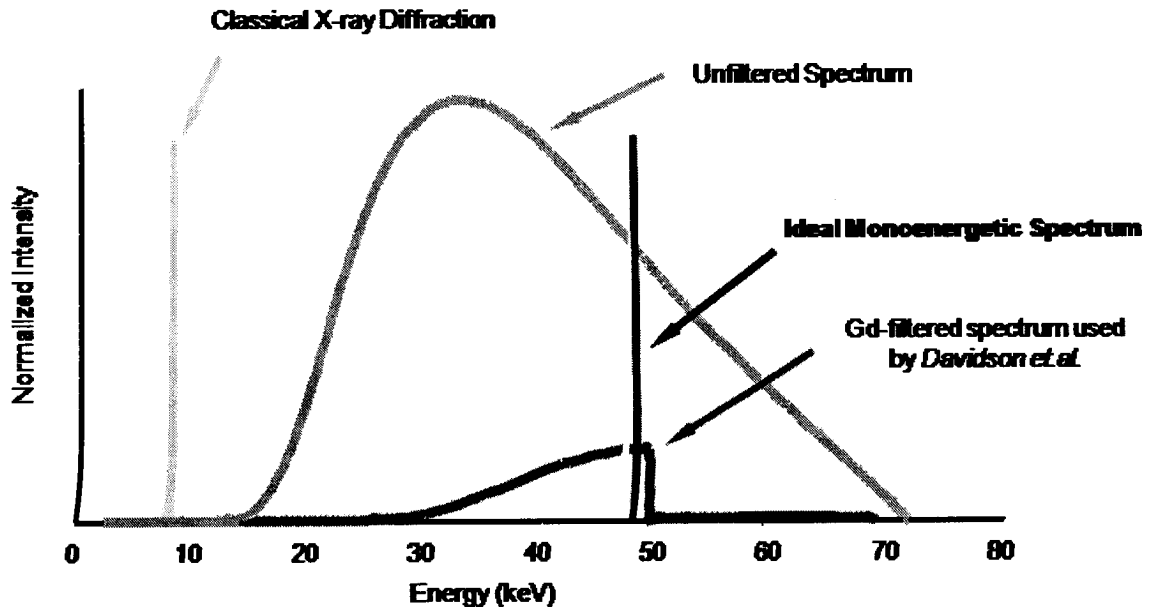

Fig. 1.8: Spectra of various x-ray sources.

and may be almost monoenergetic.

As will be shown later in this thesis, for the geometries required to realize a CSCT system, the system angular blur is proportional to x-ray source size. This restricts source size to roughly 0.1cm^2. Such a small area would require a radioisotope of extremely high specific activity to produce sufficient photon fluence for the measured scatter to reach a usable SNR. Unfortunately, greater fluence may not be gained by a thicker radioisotope sample due to self-absorption effects.

The energy of the emitted gamma rays is also a factor. Photon energies are required to be high enough for significant transmission through the specimen. Conversely, higher photon energies reduce the probability of coherent interactions in the specimen, reducing signal. A suitable radioisotope must produce gamma rays in the range of 50-100keV, as well as having a decay time constant suitable for daily use.

The lack of availability of a radioisotope which produces gamma rays in the required energy range at the specific activity required makes this technology a poor

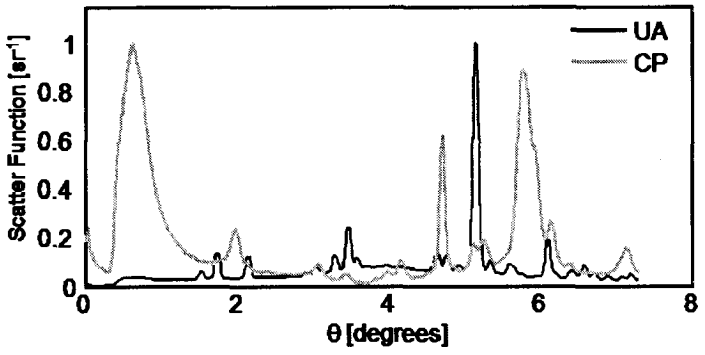

Fig. 1.9: Monoenergetic scatter functions obtained using powdered x-ray diffractometry of two kidney stone materials, uric acid (UA) and calcium phosphate(CP). Note: XRD data scaled from 8 keV to 40 keV.

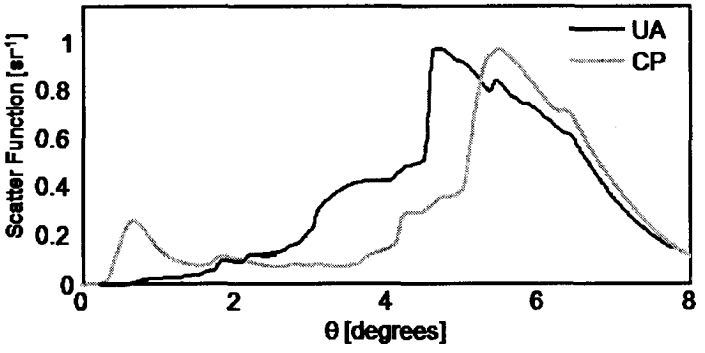

Fig. 1.10: Polyenergetic scatter functions obtained using Gd-filtered CSCT (43 keV) of two kidney stone minerals, UA and CP. Bragg-peak overlap decreases the accuracy and specificity of the material analysis.

choice for coherent scatter imaging.

Synchrotron Radiation

Synchrotrons are charged particle accelerators that can be used to produce extremely high intensity, monoenergetic x-ray beams.[64] Photon energy is tunable across a wide range through the use of Bragg monochromators, and the small focal spot sizes needed for CS imaging are available.

Although synchrotrons are ideal for coherent-scatter imaging, they have a num-

Photon Source	Photon Energy [keV]	Half Life	Specific Activity [Bq/g]	Photons in 1mm^2 beam at 35cm [photons/sec]
I-125	35	60 days	6.3×10^{14}	1.4×10^5
Pb-210	47	21 years	3.3×10^{12}	9.3×10^2
Ho-166	81	27 hours	2.6×10^{16}	8.2×10^6
Co-57	122	270 days	3.2×10^{14}	1.6×10^6
Tc-99m	140	6 hours	1.9×10^{14}	1.2×10^9
X-ray source used by *Davidson et al.*	~43	N.A.	N.A.	7.1×10^7

Table 1.2: Possible radioisotopes, their specific activities,[62] half lives,[63] and calculated fluence compared with CSCT system employed by Davidson *et al.*, which employed a conventional x-ray source with gadolinium filter.

ber of practical drawbacks disfavoring their use for coherent-scatter imaging at the present time. First, there are a limited number of beamlines available; as of 2008, there are around 50 synchrotrons operating worldwide.[65] Secondly, they are extremely expensive, with costs on the order of $100-200 million (USD) to build. Although smaller-scale light sources are being developed, it may be some time before synchrotrons are economically feasible in a commercial environment.

That said, the wide range of beam energies available, and the narrow spectral width and high intensity of synchrotrons provide a useful tool for exploring the limits of coherent-scatter imaging. However, at present, current-generation synchrotrons are not a coherent-scatter imaging solution available for widespread deployment.

Bragg monochromator with diagnostic x-ray tube

It may be possible to reduce the spectral width of the imaging beam with the addition of a Bragg monochromator to the CSCT setup.[66] Such monochromators contain highly oriented crystal structures to efficiently diffract x rays only at angles satisfying the Bragg relation. If the specimen is placed at a fixed angle from the crystal, then it follows from the Bragg relationship in Eq. (1.2) that only x-rays of

select wavelengths will satisfy the Bragg conditions to diffract off the crystal and proceed to the specimen.

Use of a source (x-ray tube focal spot) with a non-zero extent will result in a range of incident angles with respect to the crystal planes that will satisfy the Bragg relationship over a small range of x-ray energies, resulting in a "pseudo-monoenergetic" beam. X-ray wavelength λ [nm] and energy E [keV] are related by:

$$\lambda = \frac{hc}{E} \approx \frac{1.24}{E}, \tag{1.3}$$

giving

$$E = \frac{1.24}{2d\sin(\theta/2)} \tag{1.4}$$

for $n = 1$. The spectral width can be determined by differentiating with respect to θ. Davidson[67] has shown that a relative spectral width of approximately 4% can be achieved using a graphite crystal.

The reflection efficiency of any potential monochromator may be an issue for CS imaging. Monochromators are made of a variety of materials, such as graphite, silicon and germanium, with reflection efficiencies of 5 to 15%.[68] Whether these efficiencies reflect sufficient numbers of photons for coherent-scatter imaging remains to be seen. Furthermore, the added instrumentation required for implementation, such as actively correcting for temperature or vibration, and precisely aligning the crystal with the specimen add complications and reduce the mechanical robustness. These challenges aside, coherent-scatter imaging using Bragg monochromators presents a reasonable avenue for future investigation.

1.3 Balanced filters for pseudo-monoenergetic coherent scatter imaging

In 1926 Ross [69] pioneered a subtraction method to cancel out x rays in a polyenergetic x-ray spectrum except for a narrow energy band. Instead of a single x-ray

exposure, two exposures are performed with the beam attenuated by two different transmission filters. If the filter materials have similar atomic numbers, and have similar widths, both transmission spectra will be nearly identical except around the K-binding energies of the two filters, as illustrated in Fig. 1.11 for thulium (Tm) and erbium (Er) filters. If the data resulting from the two independent exposures are subtracted, and the filters are similar and balanced as mentioned, the difference exposure will mainly consist of photons with a narrow energy range (Fig. 1.12), corresponding to the difference in K-binding energy of the two filter materials. In this way spectral width as low as 2% (full width at half maximum) can be achieved by selecting two filters adjacent on the periodic table.

The Ross or balanced filter technique, as it became known, found use in x-ray physics and other fields, particulary before the development of high intensity beam lines. The technique was of benefit when the low efficiency of crystal monochromators provided insufficient x-ray counts for accurate measurements, and also in applications where a broader passband of energy could be tolerated.

The technique was further refined by Kirkpatrick *et al.* [70] who discussed filter balancing methods and the use of additional filters to improve subtraction of residuals outside the passband. Boonstra [71] carried this optimization even further, comparing fixed-time versus fixed-count measurements. Soules *et al.* [72] found that optimized Ross filters measured the attenuation coefficient of aluminum to within 1% of a calcite Bragg monochromator.

Bol [73] addressed the issue of not just balancing the filters for a given thickness, but also gave insight into choosing optimal overall filter width. This work was the foundation for optimization techniques that followed and for the optimization technique used in this thesis. Bol also addressed the issue of fluorescent radiation from the filters themselves, finding it to be insignificant if any degree of pre- and post-collimation is used.

Whereas previous investigators used a theoretical process to calculate optimal

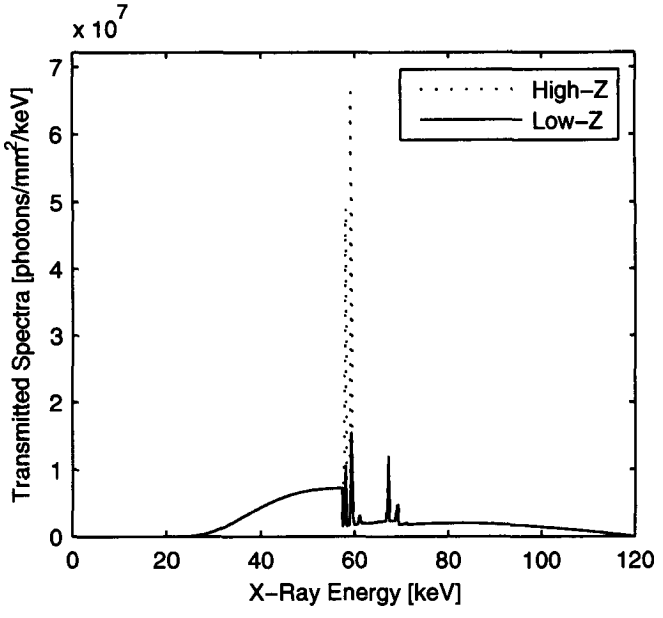

Fig. 1.11: Theoretical transmission spectra modeled using a tungsten anode x-ray tube (120 kVp) filtered by thulium (High-Z) and erbium (Low-Z) filters.

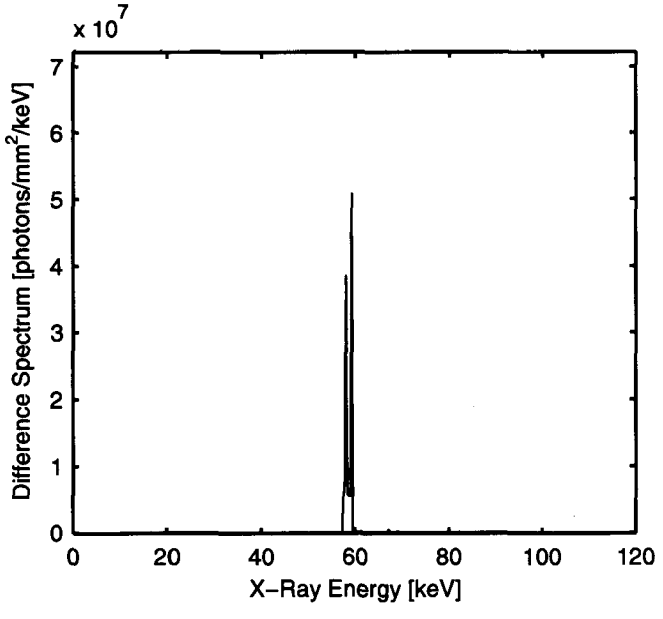

Fig. 1.12: Theoretical transmission spectrum calculated by taking the difference of the High-Z and Low-Z transmitted spectra. The majority of counts in the difference spectrum is composed of photons having energies within the K-edge discontinuity between each filter.

filter thickness, Gerrits and Bol [74] described an empirical method of determining and proving optimal filter balance. They did this by imaging a liquid which fluoresces at an energy near but not within the filter passband. They then compared the resulting 'monoenergetic' balanced filter cross section with the theoretical expected for that liquid. Superficially they looked at the ratio of the scatter intensity between two points on the scatter curve. They argued that differences in the measured ratio versus the theoretical ratio is due to unmatched transmission of the balanced filters, and thus the thickness of one filter should be adjusted until this ratio matches the theoretical ratio.

The previous studies involve photon counters or ion chambers. Motzfeld *et al.* [75] and others applied balanced filters to photographic exposures, although they noted that there are significant sources of noise with this approach. For example, emulsion thickness can vary from screen to screen, contributing significant uncertainty to the difference image. However, the rise of digital direct-conversion and CCD/CMOS optically coupled detectors eliminates these issues.

This study uses an x-ray image intensifier coupled to a CCD video camera, to record small-angle scatter patterns. Image intensifiers have a quantum efficiency near 0.5 (depending on energy) and come close to being able to detect a single photon interaction event when used with a high-quality video camera. Balanced filters are evaluated for use in pseudo-monoenergetic scatter-pattern measurements.

1.4 Research objectives

The goal of this thesis was to develop the use of balanced filters to produce pseudo-monoenergetic scatter functions for coherent-scatter imaging. Reduced angular blur will reduce overlap of Bragg peaks in CSCT imaging, thereby making it easier to identify peaks, particularly in the presence of unknown materials. To achieve this, 5 specific objectives are addressed:

1. Develop a theoretical model to identify the dominant factors determining angular blur in the CSCT prototype system

2. Design and implement the balanced filter method to produce pseudo-monoenergetic scatter functions in the prototype CSCT system

3. Compare measured scatter-function blur with predictions from the theoretical model

4. Develop a method of calibrating the CSCT system such that material-specific maps show the distributions of each identified material in mass-concentration units of g/cm^3

5. Demonstrate the balanced filter method for CSCT imaging and assess practical viability of the method

References

[1] A. A. Shokeir. Renal colic: pathophysiology, diagnosis and treatment. *Eur Urol*, 39(3):241–249, Mar 2001.

[2] J. W. Sutherland, J. H. Parks, and F. L. Coe. Recurrence after a single renal stone in a community practice. *Miner Electrolyte Metab*, 11(4):267–269, 1985.

[3] C. Y. Pak. Kidney stones. *Lancet*, 351(9118):1797–1801, Jun 1998.

[4] E. W. Vahlensieck, D. Bach, and A. Hesse. Incidence, prevalence and mortality of urolithiasis in the german federal republic. *Urol Res*, 10(4):161–164, 1982.

[5] A. Trinchieri, F. Coppi, E. Montanari, A. Del Nero, G. Zanetti, and E. Pisani. Increase in the prevalence of symptomatic upper urinary tract stones during the last ten years. *Eur Urol*, 37(1):23–25, 2000.

[6] Kiriaki K Stamatelou, Mildred E Francis, Camille A Jones, Leroy M Nyberg, and Gary C Curhan. Time trends in reported prevalence of kidney stones in the united states: 1976-1994. *Kidney Int*, 63(5):1817–1823, May 2003.

[7] Fredric L Coe, Andrew Evan, and Elaine Worcester. Kidney stone disease. *J Clin Invest*, 115(10):2598–2608, Oct 2005.

[8] Athanasios N Argyropoulos and David A Tolley. Optimizing shock wave lithotripsy in the 21st century. *Eur Urol*, 52(2):344–52, Aug 2007.

[9] S. P. Dretler. Special article: calculus breakability–fragility and durility. *J Endourol*, 8(1):1–3, Feb 1994.

[10] James C Williams, Samuel C Kim, Chad A Zarse, James A McAteer, and James E Lingeman. Progress in the use of helical ct for imaging urinary calculi. *J Endourol*, 18(10):937–941, Dec 2004.

[11] M.T.M Davidson, D.L. Batchelar, B.H. Chew, J.D. Denstedt, and I.A. Cunningham. Establishing composition and structure of intact urinary calculi by x-ray coherent scatter for clinical laboratory investigations. *J Urol*, 175(6):2336–2340, 2006.

[12] T. M. Reynolds. Acp best practice no 181: Chemical pathology clinical investigation and management of nephrolithiasis. *J Clin Pathol*, 58(2):134–140, Feb 2005.

[13] Malvinder S Parmar. Kidney stones. *BMJ*, 328(7453):1420–1424, Jun 2004.

[14] G. Bihl and A. Meyers. Recurrent renal stone disease-advances in pathogenesis and clinical management. *Lancet*, 358(9282):651–656, Aug 2001.

[15] C. Sandhu, K. M. Anson, and U. Patel. Urinary tract stones–part ii: current status of treatment. *Clin Radiol*, 58(6):422–433, Jun 2003.

[16] Tiziana Meschi, Tania Schianchi, Erminia Ridolo, Giuditta Adorni, Franca Allegri, Angela Guerra, Almerico Novarini, and Loris Borghi. Body weight, diet and water intake in preventing stone disease. *Urol Int*, 72 Suppl 1:29–33, 2004.

[17] Michael Straub and Richard E Hautmann. Developments in stone prevention. *Curr Opin Urol*, 15(2):119–126, Mar 2005.

[18] Marshall L. Stoller and Maxwell V. Meng, editors. *Urinary Stone Disease*. Humana Press Inc., 2007.

[19] J.S. Lindberg and S. Sprague. Neprolithiasis: Causes and treatment. *J. Crit. Illness*, 16:446–459, 2001.

[20] C. Chaussy, W. Brendel, and E. Schmiedt. Extracorporeally induced destruction of kidney stones by shock waves. *Lancet*, 2(8207):1265–1268, Dec 1980.

[21] Brian K Auge and Glenn M Preminger. Update on shock wave lithotripsy technology. *Curr Opin Urol*, 12(4):287–90, Jul 2002.

[22] M. Daudon, C. A. Bader, and P. Jungers. Urinary calculi: review of classification methods and correlations with etiology. *Scanning Microsc*, 7(3):1081–104; discussion 1104–6, Sep 1993.

[23] Michel Daudon and Paul Jungers. Clinical value of crystalluria and quantitative morphoconstitutional analysis of urinary calculi. *Nephron Physiol*, 98(2):p31–p36, 2004.

[24] James C Williams, K. Chee Saw, Ryan F Paterson, Erin K Hatt, James A McAteer, and James E Lingeman. Variability of renal stone fragility in shock wave lithotripsy. *Urology*, 61(6):1092–6; discussion 1097, Jun 2003.

[25] M.I. Tekin L. Peskircioglu N.C. Tarhan H. Ozkardes S. Deveci, M. Coskun. Spiral computed tomography: role in determination of chemical compositions of pure and mixed urinary stones–an in vitro study. *Urology*, 64(2):237–240, Aug 2004.

[26] K. C. Saw, J. A. McAteer, A. G. Monga, G. T. Chua, J. E. Lingeman, and J. C. Williams. Helical ct of urinary calculi: effect of stone composition, stone size, and scan collimation. *AJR Am J Roentgenol*, 175(2):329–332, Aug 2000.

[27] Anno Graser, Thorsten R C Johnson, Markus Bader, Michael Staehler, Nicolas Haseke, Konstantin Nikolaou, Maximilian F Reiser, Christian G Stief, and Christoph R Becker. Dual energy ct characterization of urinary calculi: initial in vitro and clinical experience. *Invest Radiol*, 43(2):112–119, Feb 2008.

[28] S. Ramakumar, D. E. Patterson, A. J. LeRoy, C. E. Bender, S. B. Erickson, D. M. Wilson, and J. W. Segura. Prediction of stone composition from plain radiographs: a prospective study. *J Endourol*, 13(6):397–401, 1999.

[29] C. Dawson, K. Aitken, K. Ng, G. Dolke, D. Gadian, and H. N. Whitfield. Magnetic resonance imaging of urinary calculi. *Urol Res*, 22(4):209–212, 1994.

[30] N. Mandel G. Mandel, editor. *Kidney Stones: Medical and Surgical Management.* Lippincott-Raven Publishers, Philadelphia, Pa, 1996.

[31] A. Uldall. Strategies and methods for the analytical investigation of urinary calculi. *Clin Chim Acta*, 160(2):93–101, Oct 1986.

[32] M. S. Westmore, A. Fenster, and I. A. Cunningham. Angular-dependent coherent scatter measured with a diagnostic x-ray image intensifier-based imaging system. *Med Phys*, 23(5):723–733, 1996.

[33] Deidre L Batchelar, Samuel S Chun, Timothy A Wollin, James K Tan, Darren T Beiko, Ian A Cunningham, and John D Denstedt. Predicting urinary stone composition using x-ray coherent scatter: a novel technique with potential clinical applications. *J Urol*, 168(1):260–265, 2002.

[34] G Harding, J Kosanetzky, and U Neitzel. Elastic scatter computed tomography. *Phys Med Biol*, 30(2):183–186, 1985.

[35] H. E. Johns and J. R. Cunningham. *The Physics of Radiology.* Charles C. Thomas, Springfield IL, 4th edition, 1983.

[36] Brian W. King and Paul C. Johns. Measurement of coherent scattering form factors using an image plate. *Phys Med Biol*, 53(21):5977–5990, 2008.

[37] P.C. Johns and M.P. Wismayer. Measurement of coherent x-ray scatter form factors for amorphous materials using diffractometers. *Phys Med Biol*, 49(23):5233–5250, 2004.

[38] Jens Als-Nielsen and Des McMorrow. *Elements of Modern X-Ray Physics.* John Wiley & Sons, Ltd., Chichester, 2001.

[39] H. E. Johns and J. R. Cunningham. *The physics of radiology.* Charles C. Thomas, Springfield IL, 4th edition, 1983.

[40] M. von Laue. Eine quantitative prfung der theorie fr die interferenzersheinungen bei rntgenstrahlen. *Sitzungsb. D. Math.-Phys*, pages 363–373, 1912.

[41] W. L. Bragg. The diffraction of short electromagnetic waves by a crystal. *Proc. Camb. Phil. Soc.*, 17:43–57, 1913.

[42] Robert J. Leclair and Paul C. Johns. A semianalytic model to investigate the potential applications of x-ray scatter imaging. *Med Phys*, 25(6):1008–1020, 1998.

[43] Olsen K. Dragoset R.A. Chang J. Kishore A.R. Kotochigova S.A. Chantler, C.T. and D.S. Zucker. X-ray form factor, attenuation and scattering tables (version 2.1). *National Institute of Standards and Technology, Gaithersburg, MD.*, 2005.

[44] Melanie T.M. Davidson. *Imaging composition and structure of urinary calculi using x-ray coherent scatter.* PhD thesis, The University of Western Ontario, 2005.

[45] J. Kosanetzky, B. Knoerr, G. Harding, and U. Neitzel. X-ray diffraction measurements of some plastic materials and body tissues. *Med Phys*, 14(4):526–532, 1987.

[46] S H Evans, D A Bradley, D R Dance, J E Bateman, and C H Jones. Measurement of small-angle photon scattering for some breast tissues and tissue substitute materials. *Physics in Medicine and Biology*, 36(1):7–18, 1991.

[47] R. D. Speller and J. A. Horrocks. Photon scattering–a 'new' source of information in medicine and biology? *Phys Med Biol*, 36(1):1–6, Jan 1991.

[48] R. J. Leclair and P. C. Johns. Analysis of spectral blur effects in x-ray scatter imaging. *Med Phys*, 26(9):1811–1816, 1999.

[49] R. J. Leclair and P. C. Johns. X-ray forward-scatter imaging: experimental validation of model. *Med Phys*, 28(2):210–219, 2001.

[50] Robert J Leclair and Paul C Johns. Optimum momentum transfer arguments for x-ray forward scatter imaging. *Med Phys*, 29(12):2881–2890, 2002.

[51] Robert J LeClair, Michel M Boileau, and Yinkun Wang. A semianalytic model to extract differential linear scattering coefficients of breast tissue from energy dispersive x-ray diffraction measurements. *Med Phys*, 33(4):959–967, 2006.

[52] M. S. Westmore, A. Fenster, and I. A. Cunningham. Tomographic imaging of the angular-dependent coherent-scatter cross section. *Med Phys*, 24(1):3–10, 1997.

[53] I.D. Jupp, P.T. Durrant, D. Ramsden, T. Carter, G. Dermody, I.B. Pleasants, and D. Burrows. The non-invasive inspection of baggage using coherent x-ray scattering. *IEEE Trans Nucl Sci*, 47(6):1987–1994, 2000.

[54] R.D. Luggar and W.B. Gilboy. Recent developments in industrial applications of elastic scatter x-ray inspection. *Radiation Physics and Chemistry*, 1999.

[55] S A Kerr, K Kouris, C E Webber, and T J Kennett. Coherent scattering and the assessment of mineral concentration in trabecular bone. *Physics in Medicine and Biology*, 25(6):1037–1047, 1980.

[56] G. J. Royle and R. D. Speller. Low angle x-ray scattering for bone analysis. *Phys Med Biol*, 36(3):383–389, Mar 1991.

[57] Deidre L. Batchelar, Melanie T. M. Davidson, Waldemar Dabrowski, and Ian A. Cunningham. Bone-composition imaging using coherent-scatter computed tomography: Assessing bone health beyond bone mineral density. *Med. Phys.*, 33(4):904–915, 2006.

[58] C. Dawson, J. A. Horrocks, R. Kwong, R. D. Speller, and H. N. Whitfield. Low-angle x-ray scattering signatures of urinary calculi. *World J Urol*, 14 Suppl 1:S43–S47, 1996.

[59] Melanie T. M. Davidson, Deidre L. Batchelar, Sujeevan Velupillai, John D. Denstedt, and Ian A. Cunningham. Analysis of urinary stone components by x-ray coherent scatter: characterizing composition beyond laboratory x-ray diffractometry. *Phys Med Biol*, (16):3773–3786, 2005.

[60] Melanie T. M. Davidson, Deidre L. Batchelar, Sujeevan Velupillai, John D. Denstedt, and Ian A. Cunningham. Laboratory coherent-scatter analysis of intact urinary stones with crystalline composition: a tomographic approach. *Phys Med Biol*, (16):3907–3925, 2005.

[61] Anthony B. Wolbarst. *Physics of Radiology.* Medical Physics Publishing, 2nd edition, 2005.

[62] Inc. Integrated Environmental Management. Specific activities, August 2008.

[63] Peter Siegel. Gamma energy (kev), August 2008.

[64] William R. Hendee and E. Russell Ritenour. *Medical Imaging Physics (Fourth Edition).* Wiley-Liss, 2003.

[65] lightsources.org. Light source facility information, August 2008.

[66] F. L. Cambell E. B. Hughes J. N. Otis S.Wilson H. D. Zeman A. C. Thompson, J. Llacer. Computed tomography using synchrotron radiation. *Nucl. Instrum.Methods Phys. Res*, 222:319–323, 1984.

[67] Melanie T. M. Davidson. *Imaging composition and structure of urinary calculi using x-ray coherent scatter.* PhD thesis, University of Western Ontario, 2005.

[68] E. P. Bertin. *Crystals and Multilayer Langmuir-Blodgett Films Used as Analyzers in Wavelength-Dispersive X-Ray Spectrometers, Handbook of Spectroscopy*, volume 1. CRC Press, Cleveland, USA, 1974.

[69] P.A. Ross. Polarization of x-rays. *Phys Rev*, 28:425, 1926.

[70] Paul Kirkpatrick. On the theory and use of Ross filters. *Rev Sci Instrum*, 10(6):186–191, 1939.

[71] E. G. Boonstra. Statistical considerations in the design of balanced x-ray filters. *J Sci Instrum*, 42(8):563–568, 1965.

[72] Jack A. Soules, William L. Gordon, and C. H. Shaw. Design of differential x-ray filters for low-intensity scattering experiments. *Rev Sci Instrum*, 27(1):12–14, 1956.

[73] W Bol. The use of balanced filters in x-ray diffraction. *J Sci Instrum*, 44(9):736–739, 1967.

[74] G. J. A. Gerrits and W. Bol. A method for balancing Ross filters in x-ray diffraction of liquids. *J Phys E: Sci Instrum*, 2(2):175–177, 1969.

[75] V. Motzfeld and G. Herms. The measurement of x-ray intensities by means of ross filters and photographic films. *Journal of Physics E: Scientific Instruments*, (3):296–298, 1973.

Chapter 2

Pseudo-monoenergetic x-ray diffraction measurements using balanced filters for coherent-scatter computed tomography

This chapter contains material accepted for publication in Medical Physics in a paper entitled "Pseudo-monoenergetic x-ray diffraction measurements using balanced filters for coherent-scatter computed tomography" by S.R. Beath and I.A. Cunningham

2.1 Introduction

X-ray coherent scatter (CS)[1] gives rise to x-ray diffraction patterns that, even at diagnostic energies, can be used to distinguish some biological materials and provide tissue-composition information. This was shown initially by Bradley *et al.*[2, 3] and Kosanetzky *et al.*[4] The team of Johns, Leclair, Wismayer, King and colleagues built on this work to determine how best to extract this information[5, 6, 7, 8, 9] using both diffractometers[10] and imaging detectors[11] to measure this low-angle scatter from a number of materials.

Building on prior work by Harding and colleagues,[12, 13, 14] a coherent-scatter computed tomography (CSCT) facility has been developed in our laboratory.[15, 16] The CS patterns are used to generate tomographic images showing distributions of component materials. In 1996, Dawson and colleagues[17] showed that minerals in urinary calculi have characteristic CS patterns that can be used for identification. Davidson, Batchelar and colleagues in our laboratory generated tomographic images showing component-mineral distributions in intact kidney stones.[18, 19, 20]

A limitation to the use of (polyenergetic) x-ray tubes is the angular width of lines in diffraction patterns due to the x-ray spectral width.[11, 21] As a result, definitive identification of some materials can be difficult or impossible when mixed with unknown materials.

In 1926, Ross[22] introduced the "balanced filter" technique as a method of obtaining nearly monoenergetic x-ray diffraction patterns. If two transmission filters are chosen such that their atomic numbers are similar, the difference pattern is similar to a monoenergetic pattern corresponding to the average K-edge energy although blurred by a spectral width determined by the K-edge-energy difference, which we call the difference-spectrum "passband."

Application and optimization of balanced filters has since evolved. Efforts by Pierce[23] involved finding balanced filter thicknesses empirically, as did Wollan,[24]

Boonstra[25], and Gerrits and Bol.[26] A method of correcting for filter imbalances with a third filter was explored by Kirkpatrick.[27, 28]

Soules *et al.*[29] matched filter transmission to suppress a K_β characteristic line outside of the narrow passband. Bol[30] chose filter thicknesses to maximize the difference signal in the passband. Recently Saito[31] used balanced filters for monoenergetic computed tomography. His method of filter optimization included choosing an optimal filter thickness ratio that matched transmission below the passband and then filter thicknesses to maximize differential transmission in the passband. Balanced filters were popular before the development of synchrotrons and they continue to be used in the study of x-ray physics,[32] medical imaging,[33] baggage inspection[34, 35] and elsewhere.

A relative spectral root-mean-square (RMS) width of 1-2% can be achieved by selecting two filters adjacent in the periodic table of elements. However, since the method involves the difference of two measured diffraction patterns, noise in the difference pattern is often a consideration. Also, the widths of Bragg peaks are increased by other considerations that depend on instrumentation and measurement geometries.

Noise can be reduced by choosing filters that have atomic number differences (ΔZ) greater than unity at the expense of angular blur. The goal of this investigation is to examine all factors contributing to angular blur to enable appropriate filter selection and to apply this technique to coherent scatter imaging of mineral components found in kidney stones.

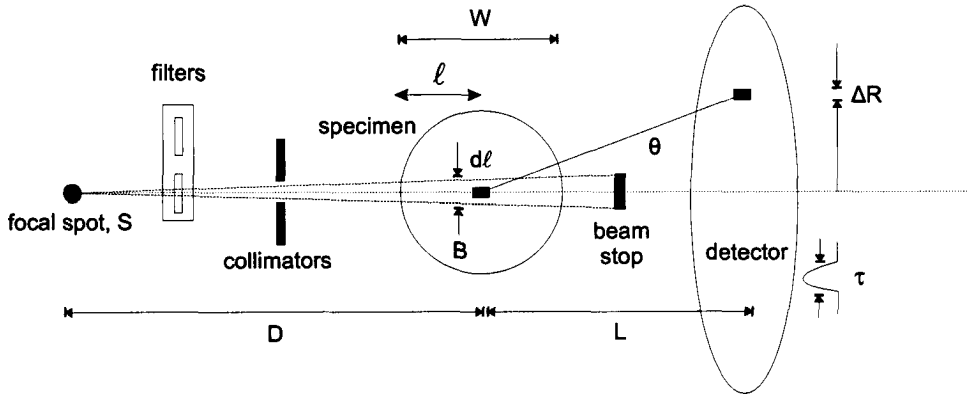

Fig. 2.1: Schematic illustration of the CSCT system.

2.2 Theory

2.2.1 Coherent scatter and scatter functions

The theoretical basis of coherent-scatter imaging has been described in detail elsewhere[1, 12, 3, 15, 11] and only a brief summary is given here. A thin "pencil" beam of x rays is incident on the specimen and fully attenuated by a beamstop placed in front of an x-ray image intensifier (XRII) as illustrated in Fig. 2.1. The detector captures a two-dimensional scatter pattern characteristic of the specimen. Many biological materials are either amorphous or polycrystalline, and coherent-scatter often shows circular symmetry similar to powder diffractometry. The number of scattered photons that leave the specimen at angle θ from position l (per unit solid angle Ω and path l through the specimen) is given by:[19]

$$\frac{\mathrm{d}^2 N_S(\theta, l)}{\mathrm{d}\Omega\, dl} = N_o T_p T_s\, n_o(l) \frac{\mathrm{d}_e\sigma(\theta, l)}{\mathrm{d}\Omega} \tag{2.1}$$

where N_o is the number of incident monoenergetic photons, T_p and T_s are transmission factors of the primary beam from specimen entrance to l and of the scattered beam from l to exit respectively, $n_o(l)$ is the volume density of electrons at l and $\mathrm{d}_e\sigma/\mathrm{d}\Omega$ is the total scatter cross section per unit solid angle per electron.[36, 10] At

low scatter angles, the majority of scatter from kidney-stone components is due to coherent-scatter interactions and we can write the product $T_p T_s \approx T$, the primary-beam transmission through the entire specimen. The small contribution from incoherent scatter adds a negligible diffuse background to scatter patterns.

For a specimen of diameter W, the differential number of scattered photons is given by:

$$\frac{\mathrm{d}N_S(\theta)}{\mathrm{d}\Omega} = \int_{-W/2}^{W/2} \frac{\mathrm{d}^2 N_S(\theta, l)}{\mathrm{d}\Omega\, \mathrm{d}l}\, \mathrm{d}l, \tag{2.2}$$

and use of the x-ray spectrum $\mathrm{d}N_o(E)/\mathrm{d}E$ gives:

$$\frac{\mathrm{d}^2 N_S(\theta, E)}{\mathrm{d}\Omega \mathrm{d}E} = \frac{\mathrm{d}N_o(E)}{\mathrm{d}E} T(E) \int_{-W/2}^{W/2} n_o(l) \frac{\mathrm{d}_e\sigma(\theta, E, l)}{\mathrm{d}\Omega}\, \mathrm{d}l. \tag{2.3}$$

When using an energy-integrating detector (such as the CsI-based XRII used in this study) to measure scatter patterns, the signal from a small detector element at a position corresponding to scatter angle θ, $d(\theta)$, is given by:

$$d(\theta) = k\, \Delta\Omega_p(\theta) \int_0^{\infty} E_{abs}(E)\, \alpha(E) \frac{\mathrm{d}^2 N_S(\theta, E)}{\mathrm{d}\Omega \mathrm{d}E}\, \mathrm{d}E \tag{2.4}$$

where k is the system gain (digital value per unit energy absorbed) generally not known, $\Delta\Omega_p(\theta) = \frac{a^2}{L^2} \cos^3\theta$ is the solid angle subtended at the center of the specimen of one detector element with area a^2, $E_{abs}(E)$ is the energy absorbed (transferred to electron kinetic energy) per interacting scattered x ray and is approximately equal to the incident photon energy minus the energies of characteristic photons that are emitted,[36] and $\alpha(E)$ is the detector quantum efficiency. Thus:

$$\begin{aligned} d(\theta) \;=\; & k \frac{a^2}{L^2} \cos^3\theta \int_{-W/2}^{W/2} n_o(l) \int_0^{\infty} E_{abs}(E)\, \alpha(E) \\ & \times \frac{\mathrm{d}N_o(E)}{\mathrm{d}E} T(E) \frac{\mathrm{d}_e\sigma(\theta, E, l)}{\mathrm{d}\Omega} \mathrm{d}E\, \mathrm{d}l. \end{aligned} \tag{2.5}$$

The line integral over l in Eq. (2.5) is of particular importance, but is made complicated by the dependence of many terms on x-ray energy. For the special case

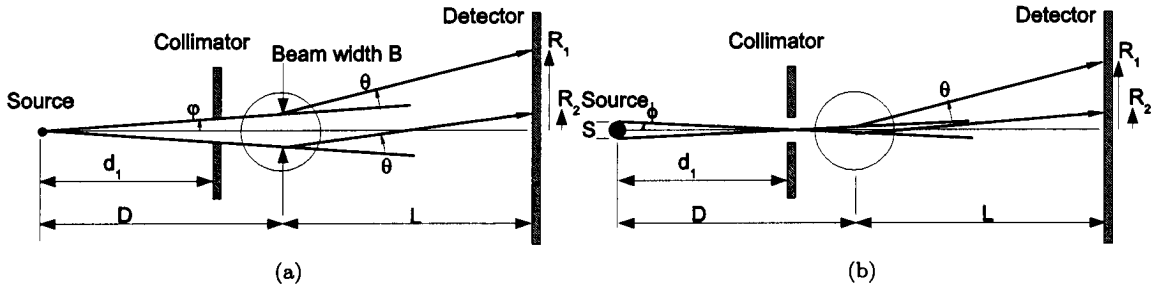

Fig. 2.2: (a) Radiation coming from a point source forming a beam of nominal width B at the specimen will result in broadening of a Bragg peak at angle θ between R_1 and R_2 on the detector. Angles are exaggerated for clarity. (b) A Bragg peak at angle θ will be distributed between R_1 and R_2 due to the finite source size S.

of N_o monoenergetic incident photons having energy E_o, we obtain:

$$\begin{aligned} d(\theta)|_{E_o} &= kN_oE_{abs}(E_o)\alpha(E_o)T(E_o)\frac{a^2}{L^2}\cos^3\theta \\ &\quad \times \int_{-W/2}^{W/2} n_o(l)\frac{\mathrm{d}_e\sigma(\theta, E_o, l)}{\mathrm{d}\Omega}\mathrm{d}l. \end{aligned} \tag{2.6}$$

The integrand is labeled the linear differential coherent-scatter coefficient, γ, equal to the probability per unit solid angle and path length of a coherent-scatter interaction occurring at angle θ:

$$\gamma(\theta, l)|_{E_o} = n_o(l)\frac{\mathrm{d}_e\sigma(\theta, E_o, l)}{\mathrm{d}\Omega}. \tag{2.7}$$

Next, a linear coherent-scatter function $\mathrm{C}(\theta)$ is defined as a function of position through the specimen:

$$\mathrm{C}(\theta, l)|_{E_o} \equiv kN_oE_{abs}(E_o)\alpha(E_o)\ \gamma(\theta, l)|_{E_o} \tag{2.8}$$

and line integrals of $\mathrm{C}(\theta, l)|_{E_o}$, denoted by $\mathrm{C}_{\mathrm{int}}(\theta)|_{E_o}$, are given by

$$\begin{aligned} \mathrm{C}_{\mathrm{int}}(\theta)|_{E_o} &\equiv kN_oE_{abs}(E_o)\alpha(E_o)\int_{-W/2}^{W/2}\gamma(\theta, l)|_{E_o}\mathrm{d}l \\ &= \frac{d(\theta)}{\frac{a^2}{L^2}\cos^3\theta\, T(E_o)}. \end{aligned} \tag{2.9}$$

This equation shows that for a monoenergetic spectrum, $\mathrm{C}_{\mathrm{int}}(\theta)$ is proportional to line integrals of the differential scatter cross section $\mathrm{d}_e\sigma/\mathrm{d}\Omega$ and can be determined from

measurements of $d(\theta)$ and transmission T, where T is measured using the transmitted primary beam with a detector placed on the beamstop in Fig. 2.1. In our work, polyenergetic beams are used and therefore measurements of $C_{int}(\theta)$ and $d(\theta)$ are weighted by the spectrum of scattered x rays and the CsI detector response, while measurements of T are weighted by the incident spectrum and the Gd_2O_2S detector response. This approximation is thought to be acceptable as measured transmission factors are always greater than 0.9 and thus minor errors in estimates of T will have little impact on calculations of $C_{int}(\theta)$.

In the CSCT system, $C_{int}(\theta)$ is measured over a range of positions and azimuthal angles ϕ in a plane through the specimen. This corresponds to first-generation CT geometry[37] and filtered-backprojection reconstruction is used to determine values of the linear scatter function, $C(\theta)$, at each pixel location in a tomographic slice. In this article, we describe an investigation of Bragg-peak width as it pertains to CSCT imaging.

2.2.2 Causes of scatter-function blur

Diffraction at angle θ (twice the Bragg angle) of x rays having wavelength λ from crystal planes with spacings d is governed by the Bragg relationship:[38] $n\lambda = 2d\sin(\theta/2)$. Only first-order diffraction ($n = 1$) is considered here. Use of a broad spectral width and other experimental considerations result in a broadening of Bragg peaks corresponding to increased angular blur in $C_{int}(\theta)$. Starting with a simplified one-dimensional geometry and a point source of x rays, these mechanisms are described using approximate relationships to identify major factors contributing to angular blur.

Geometric considerations

The specimen is irradiated with a small diverging beam having nominal width B at the specimen, defined by a collimator placed a distance d_1 from the source, as illustrated in Fig. 2.2(a). Assuming a monoenergetic point source, a ray traveling along the beam top leaves the source at angle φ from the central axis and is scattered by angle θ in the specimen, reaching the detector at position $R_1 = B/2 + L\tan(\varphi+\theta)$ where φ is the beam divergence half-angle given by $\tan\varphi = \frac{B/2}{D}$. Using a small-angle approximation ($\varphi < 0.1°$ and $\theta < 10°$) gives $\tan(\varphi+\theta) \approx \tan\varphi + \tan\theta$ and thus scatter at θ may reach the detector anywhere over a range $\Delta R_B = R_1 - R_2 \approx 2(L+D)\tan\varphi = (L+D)B/D$, corresponding to a Bragg-peak RMS width of σ_B where:

$$\sigma_B = \frac{1}{\sqrt{12}}\frac{\Delta R_B}{L} \approx \frac{1}{\sqrt{12}}\left(\frac{L+D}{LD}\right)B. \tag{2.10}$$

The $1/\sqrt{12}$ term results from calculating the RMS width of a rectangular distribution.

Source size S also introduces blur in θ as illustrated in Fig. 2.2(b) where a ray coming from the bottom of the focal spot and passing through the center of the collimator opening is scattered in the specimen by θ and incident on the detector at $R_1 = (D-d_1)\tan\phi + L\tan(\phi+\theta)$ where ϕ is the source half-angle given by $\tan\phi = \frac{S/2}{d_1}$. Thus, scatter at θ is blurred over a distance $\Delta R_S \approx (L+D-d_1)S/d_1$ on the detector, resulting in a Bragg-peak RMS width σ_S where:

$$\sigma_S \approx \frac{1}{\sqrt{12}}\left(\frac{L+D-d_1}{Ld_1}\right)S. \tag{2.11}$$

By using the small-angle approximation and choosing the paths to converge at the collimator position in this calculation, focal-spot blur is shown to act independently of, and in addition to, beam-width blur.

Large specimens introduce a rectangular broadening of Bragg peaks due to variations in the scatter-event position along path l. For a specimen of diameter W, scatter may be incident on the detector over a range $\Delta R_W = W\tan\theta \approx W\theta$, corresponding

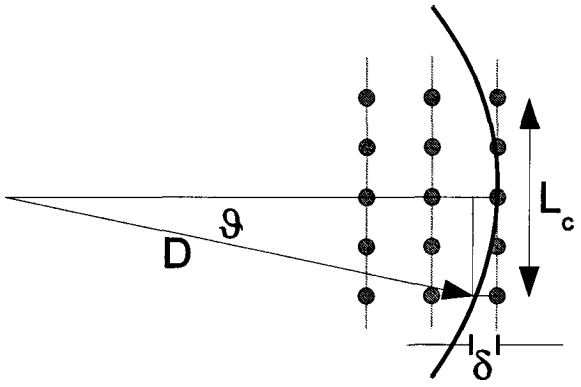

Fig. 2.3: Curvature of the spherical wavefront coming from a point source at distance D restricts the scattering centers that contribute to the interference pattern to the lateral extent L_c.

to an RMS width σ_W given by:[15]

$$\sigma_W \approx \frac{1}{\sqrt{12}} \frac{W\theta}{L}. \tag{2.12}$$

Spatial resolution of the imaging detector results in a small additional blur of scatter patterns. The system line-spread function was measured (slanted-edge method[39]) and shown to be approximately Gaussian with an RMS width of $\tau = 0.24$ mm (including the effect of pixel size), giving:

$$\sigma_\tau \approx \frac{\tau}{L}. \tag{2.13}$$

The measured scattered signal $d(\theta)$ is determined from images of scatter patterns $d_{i,j}$ (where i, j are row and column pixel indices) by averaging pixel values in concentric rings of nominal width one pixel x_o. Linear interpolation of $d_{i,j}$ to the nearest ring introduces an additional rectangular blur by approximately x_o, corresponding to an increase in Bragg-peak RMS angular width of σ_R, where:

$$\sigma_R \approx \frac{1}{\sqrt{12}} \frac{x_o}{L}. \tag{2.14}$$

Coherence considerations

At diagnostic x-ray energies, multiple x-ray interactions are highly unlikely and the kinematical approximation is used,[40] making both the width and height of Bragg peaks depend on the number of lattice atoms contributing to interference patterns in a simple way. This is determined by crystal size for small crystals when using a highly coherent beam,[41] and potentially by curvature of the spherical wavefront radiating from a point source as illustrated in Fig. 2.3. Interference effects (even with a single x-ray photon) may occur from scattering centers over a region of up to lateral dimension L_c for which the wavefront is approximately in phase. In Fig. 2.3, this requires δ be a small fraction of λ. Thus, choosing $\delta = \lambda/4$ gives the condition $\delta = D(1 - \cos\vartheta) = \lambda/4$. Since $\sin\vartheta = \frac{L_C/2}{D} \approx \vartheta$ and $\frac{\lambda}{4D} \ll 1$, we obtain

$$L_c \approx 2D \arccos\left(1 - \frac{\lambda}{4D}\right) \approx 2D\sqrt{1 - \left[1 - \frac{\lambda}{4D}\right]^2} \approx \sqrt{2D\lambda} \tag{2.15}$$

to a very good approximation. Small values of L_c result in broadening of Bragg peaks as described by the Scherrer formula[41] where the peak full-width at half-maximum (FWHM) is given by:[41]

$$\mathrm{FWHM}_C \approx \frac{0.9\lambda}{L_C \cos\theta}. \tag{2.16}$$

For small θ, peak shape is approximately proportional to $\mathrm{sinc}^2\theta$.[40] Although the RMS width of a squared sinc function is undefined, the RMS width σ of a Gaussian peak is related to its FWHM by $\sigma = 1/\sqrt{8\ln 2} \times$ FWHM. Approximating the central region of $\mathrm{sinc}^2\theta$ as a Gaussian curve having the same FWHM and height gives the Bragg peak RMS width as:

$$\sigma_C \approx \frac{1}{\sqrt{8\ln 2}} \times \frac{0.9\lambda}{L_C \cos\theta} \approx \frac{1}{4\sqrt{\ln 2}} \sqrt{\frac{\lambda}{D}}. \tag{2.17}$$

At 40 keV, $\lambda \approx 0.031$ nm giving $L_c \approx 5$ μm. Thus, crystallites larger than 5 μm will result in Bragg peaks with an RMS width $\sigma_C \approx 2.4 \times 10^{-6}$ rad (0.00014°) at $\theta = 5°$. It will be shown below that Bragg peaks are blurred by $\sigma \approx 0.1°$ or more from other

causes in our measurements, and thus coherence considerations will impact on our measurements only for crystallites less than approximately $L_{min} \approx \lambda/(\sigma\sqrt{8\ln 2}) \approx$ 7 nm which is not a practical limitation.

Spectral-width considerations

Blur caused by the spectral width, assuming a relatively narrow spectrum, is obtained by writing the Bragg relationship as $\sin(\theta/2) = \lambda/2d = hc/2Ed$ and differentiating with respect to E. For a rectangular spectral width ΔE, the Bragg-peak RMS width is given by:

$$\sigma_E \approx \frac{2\Delta E \sin(\theta/2)}{\sqrt{12}E\sqrt{1-4\sin^2(\theta/2)}} \approx \frac{\Delta E\,\theta}{\sqrt{12}\,E}. \tag{2.18}$$

Total scatter-function blur

Each blurring mechanism described above contributes to the broadening of Bragg peaks. While blur is a function of θ for some mechanisms, the extent of each blur for a specified Bragg peak can be approximated as being constant over the width of the blurred peak, and thus each blur can be represented as a convolution integral for specified θ. Since the RMS width of a line blurred by a cascade of convolutions is the quadrature sum of the RMS width of each blurring kernel, the expected Bragg-peak RMS width in the measured scatter functions is given by σ_θ where:

$$\sigma_\theta^2 \approx \sigma_B^2 + \sigma_S^2 + \sigma_W^2 + \sigma_\tau^2 + \sigma_R^2 + \sigma_C^2 + \sigma_E^2. \tag{2.19}$$

While overall blur is the quadrature sum of these components, several components depend on both L and D, and overall blur may depend strongly on these values. As a result, the impact of changes in these two parameters are not independent of each other.

It should be noted that both σ_W and σ_E increase with θ, resulting in Bragg peaks being broadened more on the high-θ side and therefore an increase in the peak centroid

position. This effect was ignored in the above theoretical description and suggests that measured peaks may be shifted slightly toward larger θ values than predicted.

2.2.3 Pseudo-monoenergetic scatter functions using balanced filters

The balanced-filter method utilizes two elemental transmission filters, having similar K-edge energies, placed near the source. The spectrum transmitted through the low-Z filter is given by:

$$\frac{\mathrm{d}N_L(E)}{\mathrm{d}E} = \frac{\mathrm{d}N_o(E)}{\mathrm{d}E} e^{-\left(\frac{\mu}{\rho}\right)_L(E)\,\rho_L t_L}, \tag{2.20}$$

where $(\mu/\rho)_L$, ρ_L and t_L are the mass attenuation coefficient, mass density and thickness of the low-Z filter. A similar equation can be written for the high-Z filter. Integral scatter functions corresponding to use of high and low-Z filters are represented as $\mathrm{C}_H(\theta)$ and $\mathrm{C}_L(\theta)$ respectively, and the desired pseudo-monoenergetic scatter function, $\mathrm{C}_{\mathrm{int}}(\theta)$, is given by:

$$\mathrm{C}_{\mathrm{int}}(\theta) = \mathrm{C}_H(\theta) - \mathrm{C}_L(\theta). \tag{2.21}$$

Optimal filter design

Filter thicknesses are chosen to match transmission at energy E_P^-, immediately below the passband (just below the low-Z K-edge energy), giving:

$$\frac{t_L}{t_H} = \frac{\mu_H(E_P^-)}{\mu_L(E_P^-)}, \tag{2.22}$$

as illustrated in Fig. 2.4 for thulium (Tm) and erbium (Er) filters, chosen to isolate the tungsten $\mathrm{K}_{\alpha 1}$ and $\mathrm{K}_{\alpha 2}$ emissions (59.32 and 57.98 keV respectively[42, 43]). Using this ratio, Bol[30], Saito[31] and others have shown that the difference in filter transmission at E_P, the average passband energy (average of K-edge energies), is maximized when:

$$t_H = \frac{1}{\mu_H(E_P) - \frac{\mu_H(E_P^-)}{\mu_L(E_P^-)}\mu_L(E_P)} \log\left(\frac{\mu_H(E_P)}{\frac{\mu_H(E_P^-)}{\mu_L(E_P^-)}\mu_L(E_P)}\right) \tag{2.23}$$

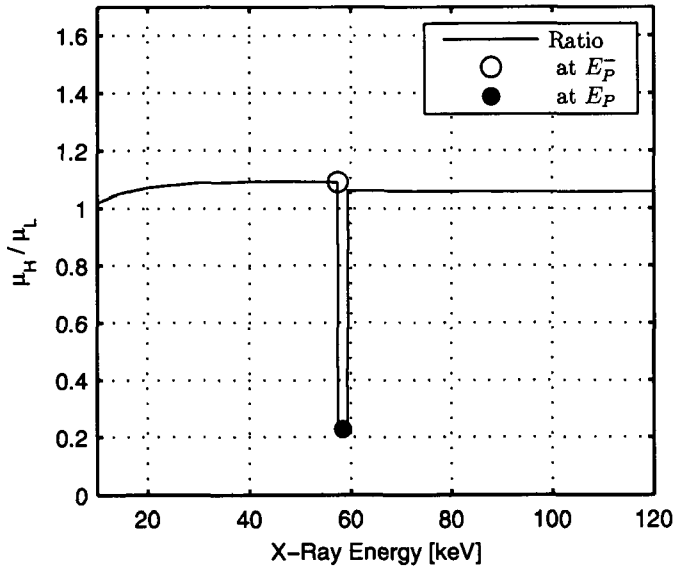

Fig. 2.4: Ratio of linear attenuation coefficients of high-Z (Tm) and low-Z (Er) filters, chosen to isolate characteristic emissions from tungsten and to minimize the difference spectrum at energy E_P^-, just below the low-Z K-edge energy and therefore just below the passband as given by Eq. (2.22).

which typically results in a filter transmission of approximately 0.3.

Figure 2.5 shows a theoretical calculation of transmitted and difference spectra from a 120 kV beam generated using our implementation of the Tucker algorithm[44] filtered with thicknesses of Tm and Er determined using Eqs. (2.22) and (2.23), chosen to isolate characteristic emissions from tungsten. Other possible filter combinations are listed in Table 2.1.

Scatter-function effective energy

The effective energy of the difference spectrum is determined primarily by the average filter K-edge energy. Potential filters are summarized in Table 2.1. The use of some filters, such as Er and Tm, will include characteristic emissions from the x-ray tube target in the passband. A more detailed calculation of the passband effective energy would take these into consideration, as well as the spectrum kV, x-ray

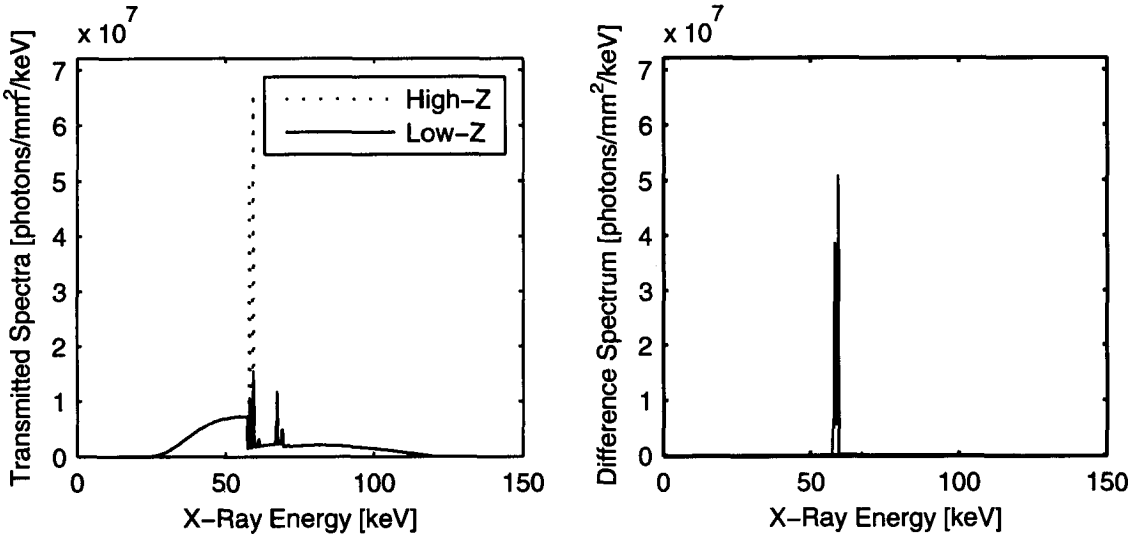

Fig. 2.5: (a) Theoretical calculation of 120 kV x-ray spectra transmitted through Tm (Z=69) and Er (Z=68) filters using thicknesses from Table 2.1. (b) Difference spectrum with average passband energy $E_P \approx 58.4$ keV and width $\Delta E_P \approx 1.9$ keV.

attenuation by the specimen, and other considerations.

Scatter-function blur

The impact on angular blur as determined by Eq. (2.19) of various source-to-object (D) and object-to-detector (L) distances using Er-Tm filters is summarized in Fig. 2.6 ($x_o = 0.28$ mm, $\tau = 0.24$ mm, $B = 0.1$ cm, tungsten target, 120 kV, W=1 cm). For the beam and focal-spot sizes used, D has an optimal value with a weak L dependence where blur is minimized. In general, D should be minimized to reduce inverse-square losses but not less than 25 or 30 cm. Increasing L always improves angular blur, but not strongly. Dimensions used in this study, unless noted otherwise, are D = 41.5 cm and L = 39.5 cm - convenient values chosen to minimize blur.

Low-Z Filter	t_L [cm]	High-Z Filter	t_H [cm]	E_P [keV]	$\frac{\Delta E_P}{E_P}$ [%]	Notes
57 - La	0.013	58 - Ce	0.010	39.7	3.8	La oxidizes in air
61 - Pm	0.016	64 - Gd	0.013	47.7	10.6	Pm is radioactive
64 - Gd	0.015	66 - Dy	0.013	52.0	6.8	
67 - Ho	0.016	69 - Tm	0.014	57.5	6.6	
68 - Er	0.015	69 - Tm	0.013	58.4	3.3	W anode Kα x-rays
72 - Hf	0.013	73 - Ta	0.009	66.4	3.1	W anode Kβ x-rays

Table 2.1: Possible balanced-filter combinations using Eqs. (2.22) and (2.23). Mean effective energy in the difference spectrum is E_P, the average K-edge energy. Spectral width is determined primarily by ΔE_P, the difference in K-edge energies.

2.3 Materials and methods

2.3.1 Coherent-scatter system description

The CSCT system consists of a tungsten-anode x-ray tube (Varian Medical Systems, Palo Alto, CA) and CsI XRII (Precise Optics, Bay Shore, NY) mounted on an optical bench using 1st-generation CT geometry as illustrated in Fig. 2.1. The x-ray beam was collimated to 1-mm square using Huber slits (XIA LLC, Hayward CA) and filtered by Tm and Er filters (ESPI Metals, Ashland, OR) located close to the tube. Both filters were 0.0127 cm thick which is very close to the optimal Bol-Saito thicknesses.

Use of filters at a non-Bol-Saito thickness ratio may result in the addition or subtraction of a background to the Bragg peaks. In our experience, this background was negligible with the filters perpendicular to the beam. In principle, one (or both) of the filters could be rotated to achieve the optimal thicknesses.

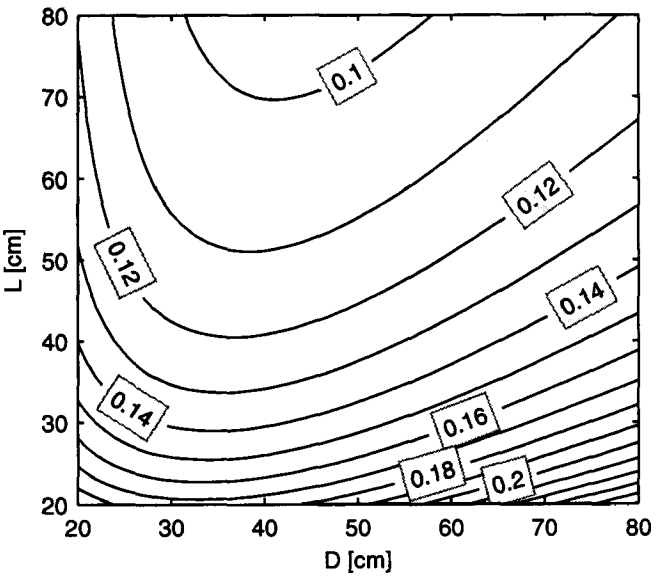

Fig. 2.6: Total theoretical RMS angular blur in degrees at $\theta = 2°$ from the test Ca stone using balanced Er-Tm filters for various source-to-object (D) and object-to-detector (L) distances.

The beam interrogates the specimen placed on a translate-rotate-elevate motorized stage. Transmitted photons are incident on a Lanex-regular screen (Kodak / Carestream, Rochester, NY) coupled to a photodiode and mounted on a beam stop. Scattered photons ($\theta < 15°$) are incident on the XRII which is coupled to a CCD FireWire camera (Prosilica, Burnaby, BC).

Images of scatter patterns were obtained after dark subtraction and correction for XRII geometric distortion.[45] Values of d_θ were determined by averaging $d_{i,j}$ values in concentric rings about the center. The integral scatter function, $C_{int}(\theta)$, was determined using Eq. (3.3). Focal-spot size (FWHM) was measured using a pin-hole camera to be 1.2 x 0.9 mm.

2.3.2 Validation of scatter-function-blur model

The theoretical model of scatter-function blur using balanced Er-Tm filters in Eq. (2.19) was validated using 0.5 cm and 1.5-cm diameter cylinders of aluminum (Al) powder (VWR International, West Chester, PA). Aluminum powder was chosen as it produces distinct Bragg peaks from which peak width can be determined experimentally and the scatter angle of each peak can be calculated theoretically. Aluminum has a face-centered cubic structure (Fm-3m, space-structure 225)[46] and cell length $a = 4.0497$ Å (App 5 of Cullity[47]). Theoretical angles of the first five Bragg peaks were determined for 58.4 keV using commercial software (Crystal Impact[48]) as indicated in Fig. 2.7(b).

2.3.3 Pseudo-monoenergetic scatter functions

Scatter patterns and functions from commercial powdered preparations of four representative kidney-stone minerals (calcium oxalate monohydrate (COM), calcium phosphate dihydrate (CPD), cystine (CYS), magnesium ammonium phosphate hexahydrate (MAP, struvite), Sigma-Aldrich Co. and Fluka Chemika), were obtained using balanced Er-Tm filters (120 kV, 300 mAs, $D = 41.5$ cm, $L = 39.5$ cm, $W = 1$ cm) to demonstrate the extent to which scatter-function peaks can be resolved. Results were compared with copper K_α x-ray diffractometry (XRD) measurements at ~ 8 keV (Rigaku Corp. MiniFlex XRD).

2.4 Results

2.4.1 Scatter-function angular blur

Figure 2.7(a) shows a pseudo-monoenergetic scatter pattern from Al powder obtained using balanced Er-Tm filters (140 kV, 192 mAs, $D = 63$ cm, $L = 55$ cm, $W = 1.5$ cm). Figure 2.7(b) shows a comparison of measured $C_{\text{int}}(\theta)$ with the least-

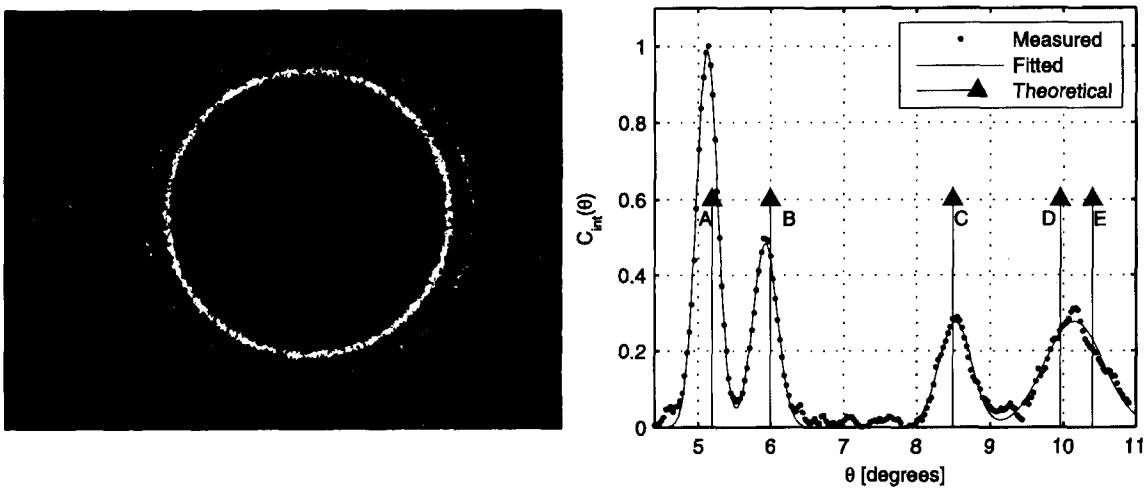

(a) (b)

Fig. 2.7: (a) Powdered-aluminum scatter pattern obtained using balanced Er-Tm filters. (b) Comparison of calculated integral scatter function, $C_{int}(\theta)$ from Eq. (3.3), with least-squares-fit curve consisting of four Gaussian peaks. Also shown are positions of the first five theoretical peaks from Al powder at 58.4 keV.

squares-fit curve and the expected positions of the first five Bragg peaks (58.4 keV). Excellent agreement was observed after stretching the theoretical angular scale by 4%, likely required due to asymmetric blur (see Sec.2.2.2) and/or imprecise knowledge of true specimen-detector distance L. Peaks D and E showed significant overlap and were fit to a single Gaussian curve.

The factors affecting angular blur in Eq. (2.19) are summarized in Fig. 2.8 for Al powder (Er-Tm filters, E_P = 58.4 keV, 140 kV, 192 mAs, D = 63 cm, L = 55 cm, W = 1.5 cm). At low scatter angles, focal-spot size and beam width are the limiting factors. Both x-ray spectral width and specimen size add blur that is proportional to θ and have an effect similar to focal spot and beam width at large angles. Detector resolution and ring interpolation add very little blur, suggesting multiple rings could be combined to reduce noise in scatter functions without degrading peak width. Coherence effects add negligible blur.

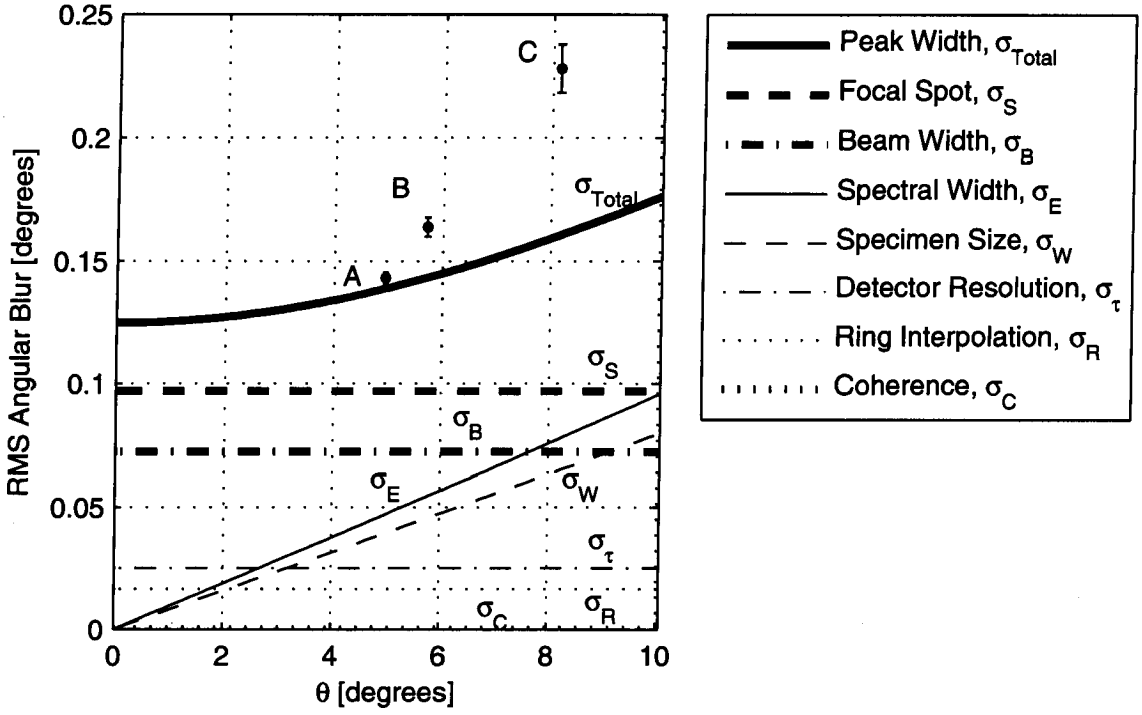

Fig. 2.8: Measured Bragg-peak RMS width for Al powder compared to the theoretical prediction given by Eq. (2.19) and its components. Under these conditions, the scatter angles 1 - 6° are most important for identifying kidney-stone minerals.

These results are specific to the test geometry indicated. For Er-Tm filters, the important Bragg peaks from kidney-stone components are between 1 and 6° where angular dependence is modest.

The measured RMS width of peaks A, B and C from powdered Al are also shown in Fig. 2.8. Measured blur is comparable to predicted blur for peaks A and B. Peak C at 8° showed a blur approximately 50% greater than predicted. While Eq. (2.19) is an approximation and complete agreement is not expected, we believe additional factors are important at larger θ such as the effects of oblique x-ray incidence, curvature of the XRII input phosphor, or off-axis electron focussing in the XRII.

Figure 2.9 shows measured and predicted RMS scatter-function blur (peak A) for various object-to-detector distances L ($W = 0.5$ and 1.5 cm Al cylinders). Increasing

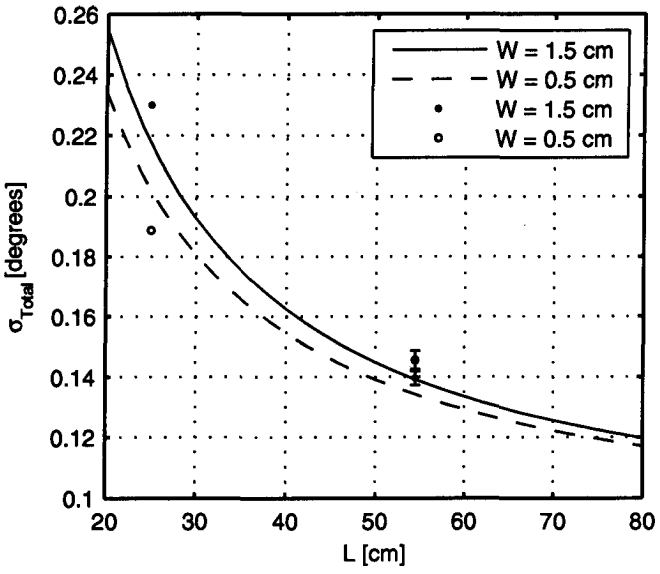

Fig. 2.9: Measured Bragg-peak RMS width for Al powder (peak A) at $L = 25$ and 55 cm compared to the theoretical prediction given by Eq. (2.19) for $W = 0.5$ and 1.5 cm (Er-Tm filters, 140 kV, 192 mAs, $D = 63$ cm). Results for $L = 55$ cm also show measurement imprecision (standard deviation in seven trials).

L decreases angular blur, whereas increasing W increases angular blur. Measured peak widths show reasonable agreement with theoretical predictions. Uncertainty in the measured peak width at $L = 55$ cm was estimated as the standard deviation of seven independent trials, and is expected to be representative of the uncertainty in all measurements.

2.4.2 Pseudo-monoenergetic scatter functions from kidney-stone minerals

Figure 2.10 shows a comparison of scatter patterns from common kidney-stone minerals obtained using XRD and balanced Er-Tm filters. While the XRD results have superior angular resolution, the balanced-filter results also show distinct rings. The XRD results required 20-min exposures while the balanced-filter results required

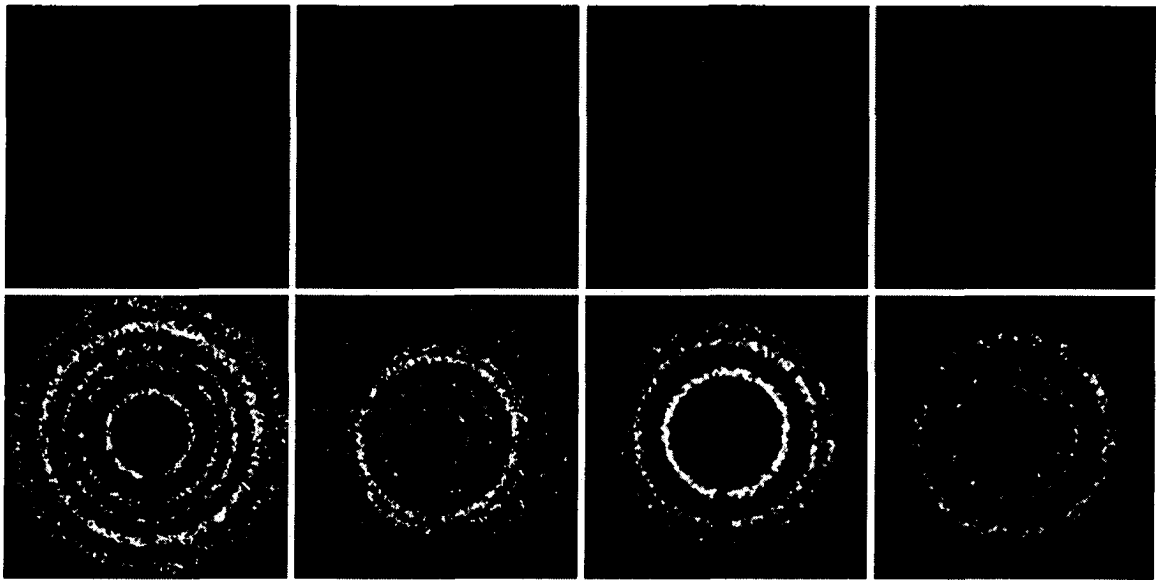

Fig. 2.10: Scatter patterns from four common kidney-stone minerals (left to right, COM, CPD, CYS, MAP). Upper: x-ray diffractometry ($\sim$ 8 keV, W = 0.5 mm). Lower: Er-Tm balanced filters (120 kV, 300 mAs, W = 1 cm, D = 42 cm, L = 40 cm).

exposures of a few seconds. Integral scatter functions from data in Fig. 2.10 are shown in Fig. 2.11. The primary peaks have an RMS width of approximately 0.15° at the lower scatter angles, consistent with expectations (Fig. 2.9).

2.5 Conclusion

It has been shown theoretically that an effective relative RMS spectral width of approximately 1% (3% rectangular blur) with a mean energy of $\sim$58 keV can be achieved using a diagnostic x-ray tube with balanced filters. Bragg-peak RMS relative width of approximately 3% at a scatter angle of 6° was observed in Al powder, consistent with a theoretical model of scatter-function blur. It is thought that at higher scatter angles, oblique incidence on the XRII curved input phosphor and off-axis electron-focussing issues may be responsible for increased blur.

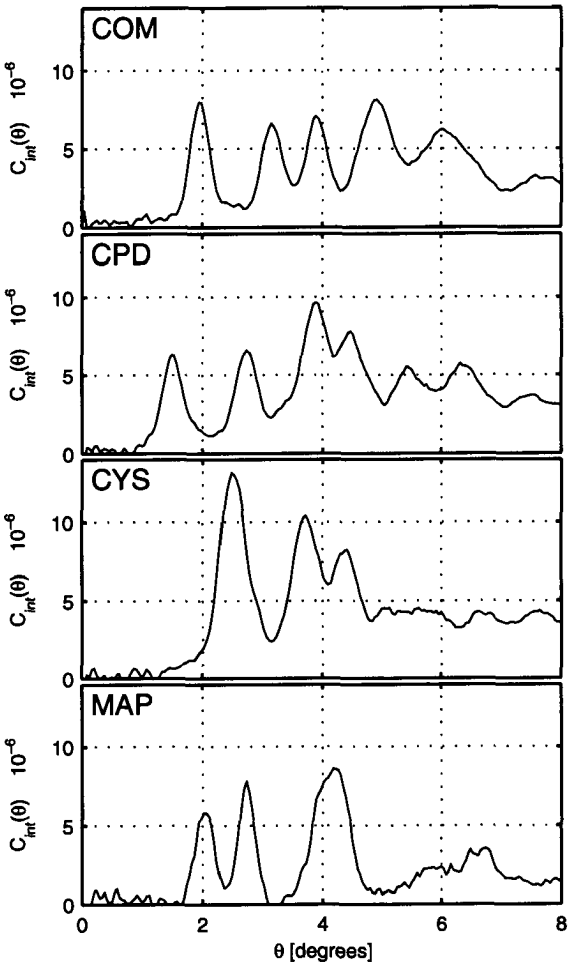

Fig. 2.11: Er-Tm scatter functions scaled by 10^{-6} as determined from scatter patterns in Fig. 2.10 (120 kV, 300 mAs, $W = 1$ cm, $D = 42$ cm, $L = 40$ cm).

As a generalization, the following additional observations are made from this work:

1. Focal-spot size and beam width are the primary considerations limiting angular blur in scatter functions.

2. The source-specimen distance should be as small as possible to maximize scatter intensity, but not less than 25 or 30 cm for a 1-mm focal spot and beam (Fig. 2.6). Blur is reduced only slowly with increasing specimen-detector distance.

3. For the conditions in this study, filter atomic number differences of two or three (Table 2.1) will maximize difference-spectrum intensity with only a minor increase in angular blur.

2.6 Acknowledgements

The authors are grateful to the Canadian Institutes of Health Research and the Lawson Health Research Institute for financial support. The assistance of Drs. Sergey Lazarev and Melanie Davidson is gratefully acknowledged.

References

[1] P. C. Johns and M. J. Yaffe. Coherent scatter in diagnostic radiology. *Med Phys*, 10(1):40–50, 1983.

[2] D. A. Bradley and A. M. Ghose. Photon scattering in biomedically important elements. *Phys Med Biol*, 29(11):1385–1397, Nov 1984.

[3] D. A. Bradley, D. R. Dance, S. H. Evans, and C. H. Jones. Quantitative measurement of small-angle gamma ray scattering from water, nylon, and lucite. *Med Phys*, 16(6):851–857, 1989.

[4] J. Kosanetzky, B. Knoerr, G. Harding, and U. Neitzel. X-ray diffraction measurements of some plastic materials and body tissues. *Med Phys*, 14(4):526–532, 1987.

[5] Robert J. Leclair and Paul C. Johns. A semianalytic model to investigate the potential applications of x-ray scatter imaging. *Med Phys*, 25(6):1008–1020, 1998.

[6] R. J. Leclair and P. C. Johns. X-ray forward-scatter imaging: experimental validation of model. *Med Phys*, 28(2):210–219, 2001.

[7] Robert J Leclair and Paul C Johns. Optimum momentum transfer arguments for x-ray forward scatter imaging. *Med Phys*, 29(12):2881–2890, 2002.

[8] Robert J LeClair, Michel M Boileau, and Yinkun Wang. A semianalytic model to extract differential linear scattering coefficients of breast tissue from energy dispersive x-ray diffraction measurements. *Med Phys*, 33(4):959–967, 2006.

[9] B. W. King and P.C. Johns. A sub-matrix method for extracting x-ray coherent scattering form factors from image plate data. *Medical Imaging 2007: Physics of Medical Imaging, Proc. SPIE*, 6510(6510):65100R.1–12, 2007.

[10] P.C. Johns and M.P. Wismayer. Measurement of coherent x-ray scatter form factors for amorphous materials using diffractometers. *Phys Med Biol*, 49(23):5233–5250, 2004.

[11] Brian W. King and Paul C. Johns. Measurement of coherent scattering form factors using an image plate. *Phys Med Biol*, 53(21):5977–5990, 2008.

[12] G Harding, J Kosanetzky, and U Neitzel. Elastic scatter computed tomography. *Phys Med Biol*, 30(2):183–186, 1985.

[13] G. Harding, J. Kosanetzky, and U. Neitzel. X-ray diffraction computed tomography. *Med Phys*, 14(4):515–525, 1987.

[14] G. Harding and B. Schreiber. Coherent x-ray scatter imaging and its applications in biomedical science and industry. *Radiation Physics and Chemistry*, 56:229–245, 1999.

[15] M. S. Westmore, A. Fenster, and I. A. Cunningham. Angular-dependent coherent scatter measured with a diagnostic x-ray image intensifier-based imaging system. *Med Phys*, 23(5):723–733, 1996.

[16] M. S. Westmore, A. Fenster, and I. A. Cunningham. Tomographic imaging of the angular-dependent coherent-scatter cross section. *Med Phys*, 24(1):3–10, 1997.

[17] C. Dawson, J. A. Horrocks, R. Kwong, R. D. Speller, and H. N. Whitfield. Low-angle x-ray scattering signatures of urinary calculi. *World J Urol*, 14 Suppl 1:S43–S47, 1996.

[18] Deidre L Batchelar, Samuel S Chun, Timothy A Wollin, James K Tan, Darren T Beiko, Ian A Cunningham, and John D Denstedt. Predicting urinary stone composition using x-ray coherent scatter: a novel technique with potential clinical applications. *J Urol*, 168(1):260–265, 2002.

[19] Melanie T. M. Davidson, Deidre L. Batchelar, Sujeevan Velupillai, John D. Denstedt, and Ian A. Cunningham. Analysis of urinary stone components by x-ray coherent scatter: characterizing composition beyond laboratory x-ray diffractometry. *Phys Med Biol*, (16):3773–3786, 2005.

[20] Melanie T. M. Davidson, Deidre L. Batchelar, Sujeevan Velupillai, John D. Denstedt, and Ian A. Cunningham. Laboratory coherent-scatter analysis of intact urinary stones with crystalline composition: a tomographic approach. *Phys Med Biol*, (16):3907–3925, 2005.

[21] R. J. Leclair and P. C. Johns. Analysis of spectral blur effects in x-ray scatter imaging. *Med Phys*, 26(9):1811–1816, 1999.

[22] P.A. Ross. Polarization of x-rays. *Phys Rev*, 28:425, 1926.

[23] W. C. Pierce. The effect of general radiation in the diffraction of x-rays by liquids. *Phys Rev*, 38:1409–1412, 1931.

[24] E. O. Wollan. Measurements of intensity of Compton modified radiation by means of filters. *Phys Rev*, 43:955–963, 1933.

[25] E. G. Boonstra. Statistical considerations in the design of balanced x-ray filters. *J Sci Instrum*, 42(8):563–568, 1965.

[26] G. J. A. Gerrits and W. Bol. A method for balancing Ross filters in x-ray diffraction of liquids. *J Phys E: Sci Instrum*, 2(2):175–177, 1969.

[27] Paul Kirkpatrick. On the theory and use of Ross filters. *Rev Sci Instrum*, 10(6):186–191, 1939.

[28] Paul Kirkpatrick. Theory and use of Ross filters. II. *Rev Sci Instrum*, 15(9):223–229, 1944.

[29] Jack A. Soules, William L. Gordon, and C. H. Shaw. Design of differential x-ray filters for low-intensity scattering experiments. *Rev Sci Instrum*, 27(1):12–14, 1956.

[30] W Bol. The use of balanced filters in x-ray diffraction. *J Sci Instrum*, 44(9):736–739, 1967.

[31] Masatoshi Saito. Quasimonochromatic x-ray computed tomography by the balanced filter method using a conventional x-ray source. *Med Phys*, 31(12):3436–3443, Dec 2004.

[32] M Cooper, R S Holt, and G Harding. Elastic and Compton scattering with W K-alpha x-radiation. *J Phys E: Sci Instrum*, 18(4):354–357, 1985.

[33] Masatoshi Saito. Dual-energy approach to contrast-enhanced mammography using the balanced filter method: Spectral optimization and preliminary phantom measurement. *Med Phys*, 34(11):4236–4246, 2007.

[34] S.P. Beevor, J. Sander, I. Raitt, J.D. Burrows, and K. Mann. Non-invasive inspection of baggage using coherent x-ray scattering. In *Security and Detection, 1995., European Convention on*, pages 301–305, 1995.

[35] I.D. Jupp, P.T. Durrant, D. Ramsden, T. Carter, G. Dermody, I.B. Pleasants, and D. Burrows. The non-invasive inspection of baggage using coherent x-ray scattering. *IEEE Trans Nucl Sci*, 47(6):1987–1994, 2000.

[36] H. E. Johns and J. R. Cunningham. *The physics of radiology.* Charles C. Thomas, Springfield IL, 4th edition, 1983.

[37] Jiang Hsieh. *Computed Tomography: Principles, Design, Artifacts, and Recent Advances.* SPIE Publications, 2003.

[38] W. L. Bragg. The diffraction of short electromagnetic waves by a crystal. *Proc. Camb. Phil. Soc.*, 17:43–57, 1913.

[39] E. Samei, M.J. Flynn, and D.A. Reimann. A method for measuring the presampled mtf of digital radiographic systems using an edge test device. *Med Phys*, 25:102–113, 1998.

[40] Jens Als-Nielsen and Des McMorrow. *Elements of Modern X-Ray Physics.* John Wiley & Sons, Ltd., Chichester, 2001.

[41] A. Guinier. *X-Ray Diffraction In Crystals, Imperfect Crystals, and Amorphous Bodies.* Dover Publications, Inc. New York, 1994.

[42] R. D. Deslattes, E. G. Kessler Jr., P. Indelicato, L. de Billy, E. Lindroth, and J. Anton. X-ray transition energies: new approach to a comprehensive evaluation. *Rev Mod Phys*, 75:35–99, 2003.

[43] R. D. Deslattes, E. G. Kessler Jr., P. Indelicato, L. de Billy, E. Lindroth, J. Anton, J. S. Coursey, D. J. Schwab, C. Chang, R. Sukumar, K. Olsen, and R. A. Dragoset. X-ray transition energies (version 1.2). Available: http://physics.nist.gov/XrayTrans. National Institute of Standards and Technology, Gaithersburg, MD., 2008, Oct 24.

[44] D. M. Tucker, G. T. Barnes, and D. P. Chakraborty. Semiempirical model for generating tungsten target x-ray spectra. *Med Phys*, 18:211–218, 1991.

[45] R. Fahrig, M. Moreau, and D. W. Holdsworth. Three-dimensional computed tomographic reconstruction using a C-arm mounted XRII: correction of image intensifier distortion. *Med Phys*, 24(7):1097–1106, 1997.

[46] Mark Winter. WebElements. The University of Sheffield and WebElements Ltd., www.webelements.com, 2008.

[47] B.D. Cullity. *Elements of X-ray Diffraction.* Addison-Wesley, 1956.

[48] Klaus Brandenburg. Diamond 3.1. Crystal Impact Inc., University of Bonn, www.crystalimpact.de, 2008.

Chapter 3

Experimental validation of balanced filters for coherent-scatter computed tomography

3.1 Introduction

X-ray coherent scatter (CS)[1] gives rise to x-ray diffraction patterns that can be used to distinguish some biological materials and provide tissue-composition information. This was shown initially by Bradley *et al.*[2, 3] and Kosanetzky *et al.*[4] Building on prior work by Harding and colleagues,[5, 6, 7] a coherent-scatter computed tomography (CSCT) facility has been developed in our laboratory.[8, 9] The CS patterns are used to generate tomographic images showing distributions of components in a specimen.

A limitation to the use of (polyenergetic) x-ray tubes is the angular width of lines in diffraction patterns due to the x-ray spectral width.[10, 11] As a result, definitive identification of some materials can be difficult or impossible when mixed with unknown materials. Ross or "balanced" filters can be used as a method of obtaining nearly monoenergetic x-ray diffraction patterns from a polyenergetic.[12, 13] If two

transmission filters are chosen such that their atomic numbers are similar, the difference pattern is similar to a monoenergetic pattern corresponding to the average K-edge energy although blurred by a spectral width determined by the K-edge-energy difference, which we call the difference-spectrum "passband".[13]

These difference scatter-patterns can be used to generate pseudo-monoenergetic scatter functions. In the same way that attenuation of x rays can be measured at regular displacements and angles to form an x-ray computed tomography (CT) image, so too can scatter functions form a coherent-scatter CT image. This technique is termed coherent-scatter computed tomography, and it produces images of the material distribution throughout a specimen.

The goal of this work is to acquire two-dimensional absolute mineral mass-density distributions using a CSCT system modified to use balanced filters. Previous studies have shown relative concentrations of each material, [9, 14, 15] but *not* calibrated to a physical quantity.

The following work describes a theoretical *absolute* mass-density distribution measurement (g/cm^3) of materials in a specimen. Reference scatter functions are measured for several types of plastics found in a soft-tissue mimicking phantom. Material-specific mass density distributions of each phantom component were acquired using balanced-filter CSCT.

3.2 Theory

The linear coherent-scatter function $C(\theta)$ is defined as a function of position, l, through the specimen:[13]

$$C(\theta, l)|_{E_o} \equiv kN_o E_{abs}(E_o)\alpha(E_o)\ \gamma(\theta, l)|_{E_o}\,, \tag{3.1}$$

where k is the system gain (digital value per unit energy absorbed) generally not known, N_o is the number of incident photons, $E_{abs}(E)$ is the energy absorbed per interacting scattered x ray, and $\alpha(E)$ is the detector quantum efficiency. The integrand

is labeled the linear differential coherent-scatter coefficient, γ, equal to the probability per unit solid angle and path length of a coherent-scatter interaction occurring at angle θ:

$$\gamma(\theta, l)|_{E_o} = n_o(l)\frac{\mathrm{d}_e\sigma(\theta, E_o, l)}{\mathrm{d}\Omega}. \tag{3.2}$$

where $n_o(l)$ is the volume density of electrons at l and $\mathrm{d}_e\sigma/\mathrm{d}\Omega$ is the total scatter cross section per unit solid angle per electron.[16, 17]

The integral linear scatter function, $\mathrm{C}_{int}(\theta)$, for the special case of N_o monoenergetic incident photons having energy E_o, is given as:

$$\begin{aligned} \mathrm{C}_{\mathrm{int}}(\theta)|_{E_o} &\equiv kN_oE_{abs}(E_o)\alpha(E_o)\int_{-W/2}^{W/2}\gamma(\theta, l)|_{E_o}\mathrm{d}l \\ &= \frac{d(\theta)}{\frac{a^2}{L^2}\cos^3\theta\, T(E_o)}, \end{aligned} \tag{3.3}$$

where W is the specimen diameter, $d(\theta)$ is the signal from a small detector element at a position corresponding to scatter angle θ, $\frac{a^2}{L^2}\cos^3\theta$ is the solid angle subtended at the center of the specimen of one detector element with area a^2, L is the specimen-to-detector distance, and $T(E_o)$ is the primary-beam transmission through the entire specimen.

In a tomographic acquisition, the linear scatter function $\mathrm{C}_{int}(\theta)$ is measured for a range of scatter angles θ and acquired over a range of positions t and azimuthal angles ϕ in a plane through the specimen. Filtered-backprojection reconstruction is then used to determine $\mathrm{C}(\theta)$ values at each pixel location in a tomographic slice.[18]

Tomographic analysis is further complicated by the fact that several materials may be present at any pixel location in a slice. At diagnostic x-ray energies, coherent-scatter from a complex material is a linear superposition of scatter from its components:[9]

$$\mathrm{C}(\theta) = \sum_j \rho_j \left(\frac{\mathrm{C}}{\rho}\right)_j (\theta), \tag{3.4}$$

where ρ_j is the mass density of material j having mass coherent-scatter function

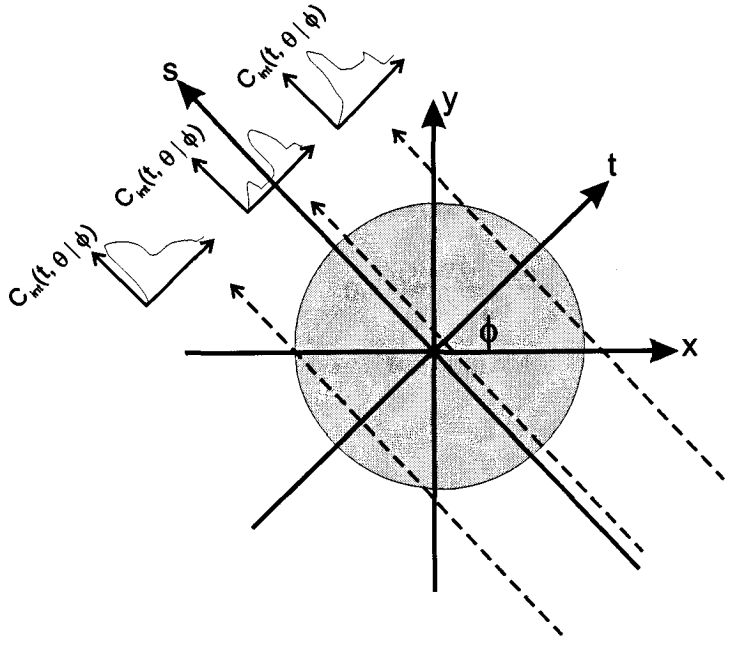

Fig. 3.1: Illustration of $C_{int}(t, \theta, \phi)$ acquisition in the 1st generation CT geometry employed by the scanner in this study. This shows both the image coordinate system (x, y) and the rotated coordinate system (s, t) for a CT projection angle ϕ.

$(\mathrm{C}/\rho)_j(\theta)$ defined from Eq. (3.1) as

$$\left(\frac{\mathrm{C}}{\rho}\right)_j(\theta) \equiv kN_0E_{abs}(E_o)\alpha(E_o)\left(\frac{\gamma}{\rho}\right)_j(\theta). \tag{3.5}$$

Concentrations of components that have identifiable coherent-scatter coefficients are determined based on a library of reference scatter functions using a non-negative least-squared (NNLS) method to minimize the X^2 value given by

$$X^2 = \sum_i \left[\sum_j \mathrm{C}(\theta_i) - \rho_j \left(\frac{\mathrm{C}}{\rho}\right)_j(\theta_i)\right]^2 \tag{3.6}$$

for discrete angles θ_i. For the special case of N_o monoenergetic incident photons having energy E_o, we obtain:

$$\begin{aligned} d(\theta)|_{E_o} &= kN_oE_{abs}(E_o)\alpha(E_o)T(E_o)\frac{a^2}{L^2}\cos^3\theta \\ &\quad \times \int_{-W/2}^{W/2} n_o(l)\frac{\mathrm{d}_e\sigma(\theta, E_o, l)}{\mathrm{d}\Omega}\mathrm{d}l, \end{aligned} \tag{3.7}$$

and when combined with Eq. (3.2) the scatter signal for reference material j having thickness W_j is

$$d_j(\theta) = kN_oE_{abs}(E_o)\alpha(E_o)T_j(E_o)\frac{a^2}{L^2}\cos^3\theta\, W_j\, \gamma_j|_{E_o,\theta}. \tag{3.8}$$

Noting that transmission of low-angle coherent-scatter through the uniform reference material is approximately equal to that of the primary x rays gives $T_j = e^{-(\frac{\mu}{\rho})_j\rho_j W_j}$ and the mass coherent-scatter function at a particular energy becomes

$$\left(\frac{\mathrm{C}}{\rho}\right)_j(\theta) = d_j(\theta)\frac{\left(\frac{\mu}{\rho}\right)_j}{-T_j\ln(T_j)\frac{a^2}{L^2}\cos^3\theta}. \tag{3.9}$$

The beauty of Eq. (3.9) is that since primary transmission T_j can be measured directly and the mass attenuation coefficient $(\frac{\mu}{\rho})_j$ can be determined theoretically for a known material and spectrum, the mass scatter function $(\frac{C}{\rho})_j$ can be determined from pure samples of each reference material without knowledge of the reference samples's true mass density or thickness. The mass-density distribution of each material in a specimen can therefore be determined in g/cm^3 by minimizing Eq. (3.6) with no empirical calibration.

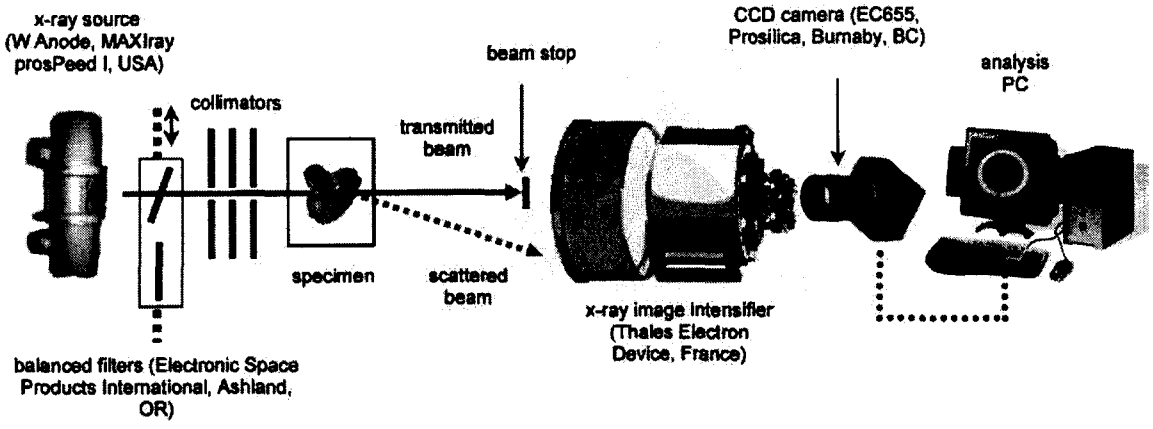

Fig. 3.2: Schematic diagram of the CSCT system.

3.3 Materials and methods

The imaging system and balanced filter setup is the same as described in Chapter 2. A diagram of this system is shown in Fig. 3.2. In addition to a single 0.3 mm gadolinium filter, balanced filters consisting of erbium and thulium (both 0.127 mm) metal foils were mounted on a translate stage such that the desired filter could be moved into the x-ray beam under computer control.

An AAPM soft-tissue mimicking low-contrast phantom, similar to that used by Harding *et al.*, Westmore *et al.* and Bachelar *et al.* was imaged in this study. As shown in Fig. 3.3, the phantom is composed of an outer PMMA cylinder of diameter 31 mm, and four 6 mm diameter rods. The composition of the rods is nylon, polycarbonate (PC), polyethylene(PE), and PMMA, respectively. Water fills the gap between the rods and the outer cylinder.

Reference scatter functions were acquired from pure 6 mm samples of the plastics and a 10 mm sample of water, at 120 kV and 403 mAs for the balanced filter acquisition and 70 kV and 400 mAs for the single-filter Gd acquisition. The source-to-object

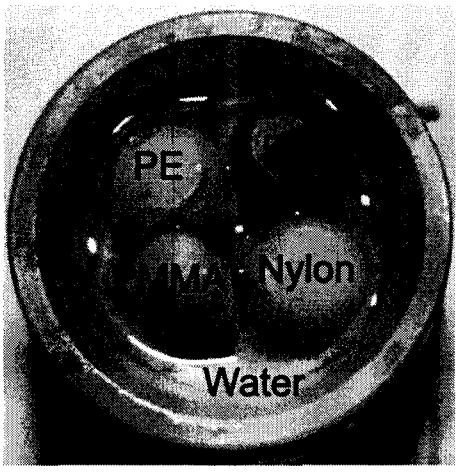

Fig. 3.3: Cross-sectional photo of the soft-tissue mimicking AAPM test phantom used in the validation of the balanced-filter CSCT system.

and object-to-detector distances were 32 cm and 35 cm respectively.

Tomographic slices through the plastic phantom were obtained by acquiring 64 scatter patterns as the object was translated through the primary beam during a 3.2 second exposure. This translation was repeated over 64 angular steps to form the 180° rotation necessary for complete CT reconstruction.

3.4 Results

Figures 3.4 - 3.6 show acquired scatter patterns of pure samples of the 5 phantom materials, obtained using erbium, thulium, and a combination of erbium and thulium filters. The patterns in Fig. 3.4 show little structure due to the large spectral width transmitted by a single filter. Some structure can be observed in Fig. 3.5, particularly in the nylon and PE samples. This is due to the sharp $K_{\alpha 1}$ and $K_{\alpha 2}$ emissions from the tungsten source which are mostly transmitted by the thulium filter but absorbed by the erbium filter. Figure 3.6 shows the difference of the Er and Tm patterns. SNR is decreased due to a smaller signal, as the signal is roughly proportional to the number of photons only in the balanced-filter passband, as well as due to an increase

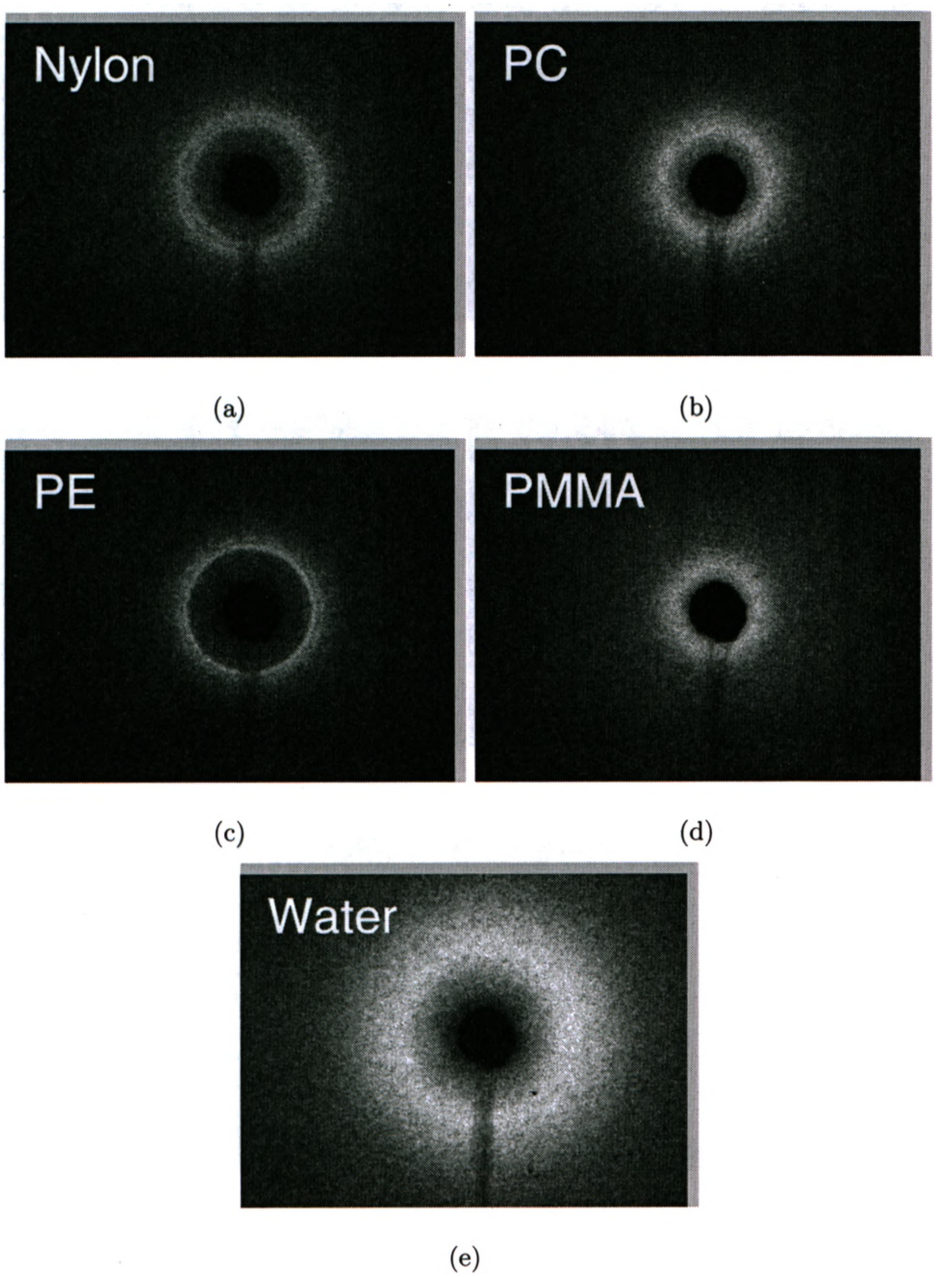

Fig. 3.5: Reference material scatter patterns obtained using an thulium filter (140 kV, 192 mAs, $D = 63$ cm, $L = 51$ cm, $W = 6$ mm for the plastics and 10 mm for water).

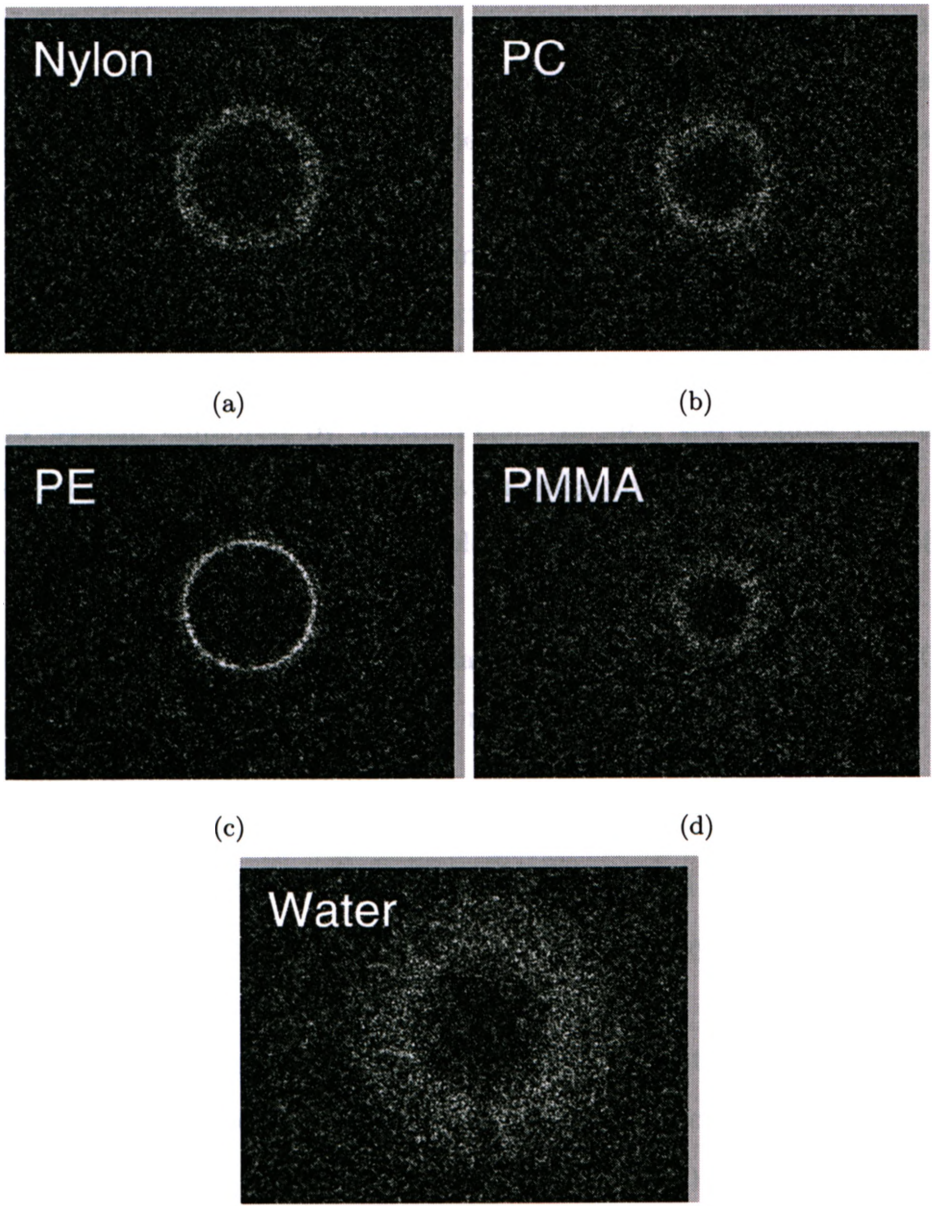

Fig. 3.6: Reference material scatter patterns obtained by subtracting the thulium filter scatter-patterns from the erbium filter scatter-patterns, producing a scatter pattern formed from photons with energies within the filter passband (effective photon energy $E_P = 58.4$ keV).

in noise (Poisson noise is additive.)

Figure 3.7 shows the integrated scatter functions calculated from the scatter patterns from Er and Tm filters recorded above. As expected, scatter peaks observed in the single-filter acquisitions are broad reflecting the wide spectral width of the x-ray spectra used.

Figure 3.8 shows the scatter-function measurements of pure samples of the plastic phantom's materials using Er-Tm balanced filters. As expected, the angular resolution of these scatter functions exceeds that of each single-filter case, as well as the CSCT system employed by Westmore[9]. In fact, the angular resolution approaches that of the traditional x-ray powder diffractometer measurements recorded by Kosanetzky[4]. In particular, the doublet in the low-angle scatter peak of nylon is visible.

Note that even with the greater angular resolution of balanced-filter CSCT, peak overlap remains a problem in the case of nylon and PE. This peak-overlap can be a cause of material misidentification.

Preliminary tomographic reconstructions of the material mass density distribution in the phantom are shown in Figures 3.9 - 3.11. Material identification accuracy is poor when a single erbium filter is used, as evidenced by the analysis incorrectly showing no nylon in the specimen. This is due to the majority of the nylon in the specimen being misidentified as PE, PMMA, and water due the similarities in main peak location and profile as seen in their respective scatter functions. However, the extra peak detail superimposed on the broad background in the thulium-filtered scatter function enables the system to make a more accurate assessment of nylon in the sample, as seen in Figure 3.11, although a significant quantity of nylon is still misidentified as PE, PMMA, and water.

It is interesting to note that the mass density distributions obtained using the single thulium filter at 120 keV is able to partially identify the nylon rod, whereas the gadolinium filtered system employed by Westmore, Batchelar and Davidson was

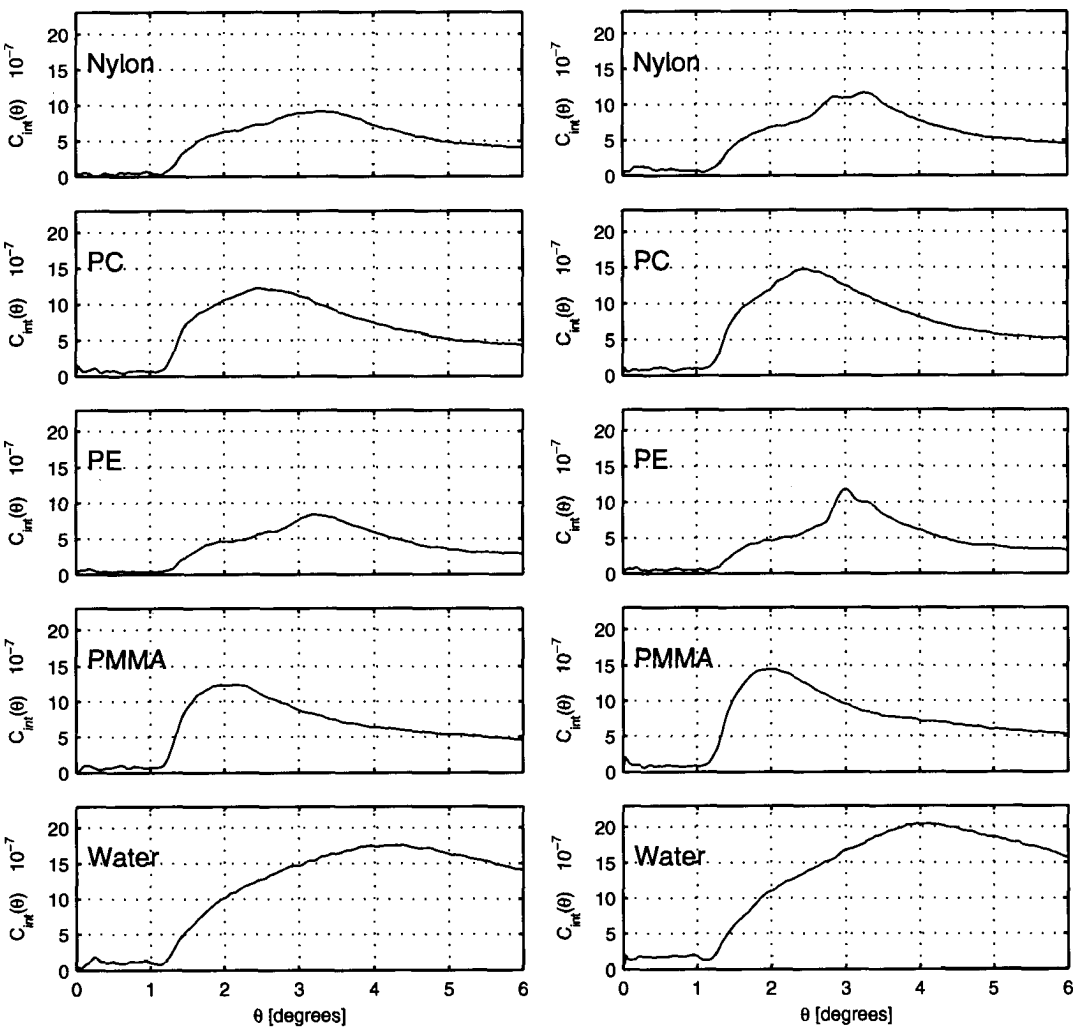

Fig. 3.7: Integral scatter functions of plastic phantom components obtained using (a) erbium and (b) thulium filters (140 kV, 192 mAs, $D = 63$ cm, $L = 51$ cm).

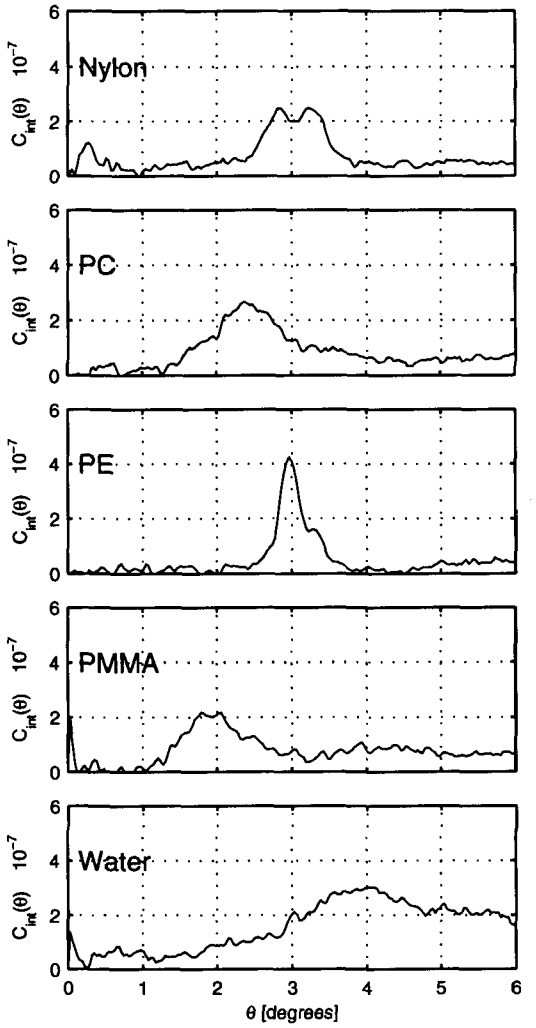

(a)

Fig. 3.8: Pseudo-monoenergetic integral scatter functions of plastic phantom components obtained using Er-Tm balanced filters (140 kV, 192 mAs, $D = 63$ cm, $L = 51$ cm).

not. Further study is needed to assess if there is a material-identification accuracy gain, or an efficiency gain, by using a thulium filter instead of gadolinium.

As expected from a soft-tissue mimicking phantom, the conventional CT cross-sections in Fig. 3.9 and Fig. 3.10 show minimal contrast, reflecting the similarity in x-ray attenuation coefficient between the plastics and water.

Figure 3.11 shows the reconstructed mass density distribution using Er-Tm balanced filters. Because of the use of balanced filters, the conventional attenuation CT image shown in Fig. 3.11 has an extremely low signal-to-noise ratio. This is due to the fact that x-ray attenuation differences in balanced-filter CT arise only from photons with energies within the filter passband. This is a small minority of photons as compared to an entire x-ray spectrum used in conventional CT, and since the attenuation coefficients of the phantom materials are similar, the resulting image has extremely low contrast. Note that the tomographic reconstruction algorithm is a work-in-progress and future improvements, such as detector binning in the specimen x and y directions (see Fig. 3.1) may increase SNR (although at the expense of in-plane resolution.)

Higher contrast is obtained when Eq. (3.9) is used to calculate mass density distributions of materials contained within the phantom from measured scatter functions. As can be seen in Fig. 3.11 the signal-to-noise ratio is sufficient to make out some details about the phantom, such as the PMMA outer container and the water infill. The SNR of the four plastics of interest appears to be too low to make out uniform objects and illuminate object borders precisely. In comparison to the CSCT imaging of the same phantom done by Westmore, the balanced filter CSCT method offers reduced signal-to-noise ratio for a similar tube load.

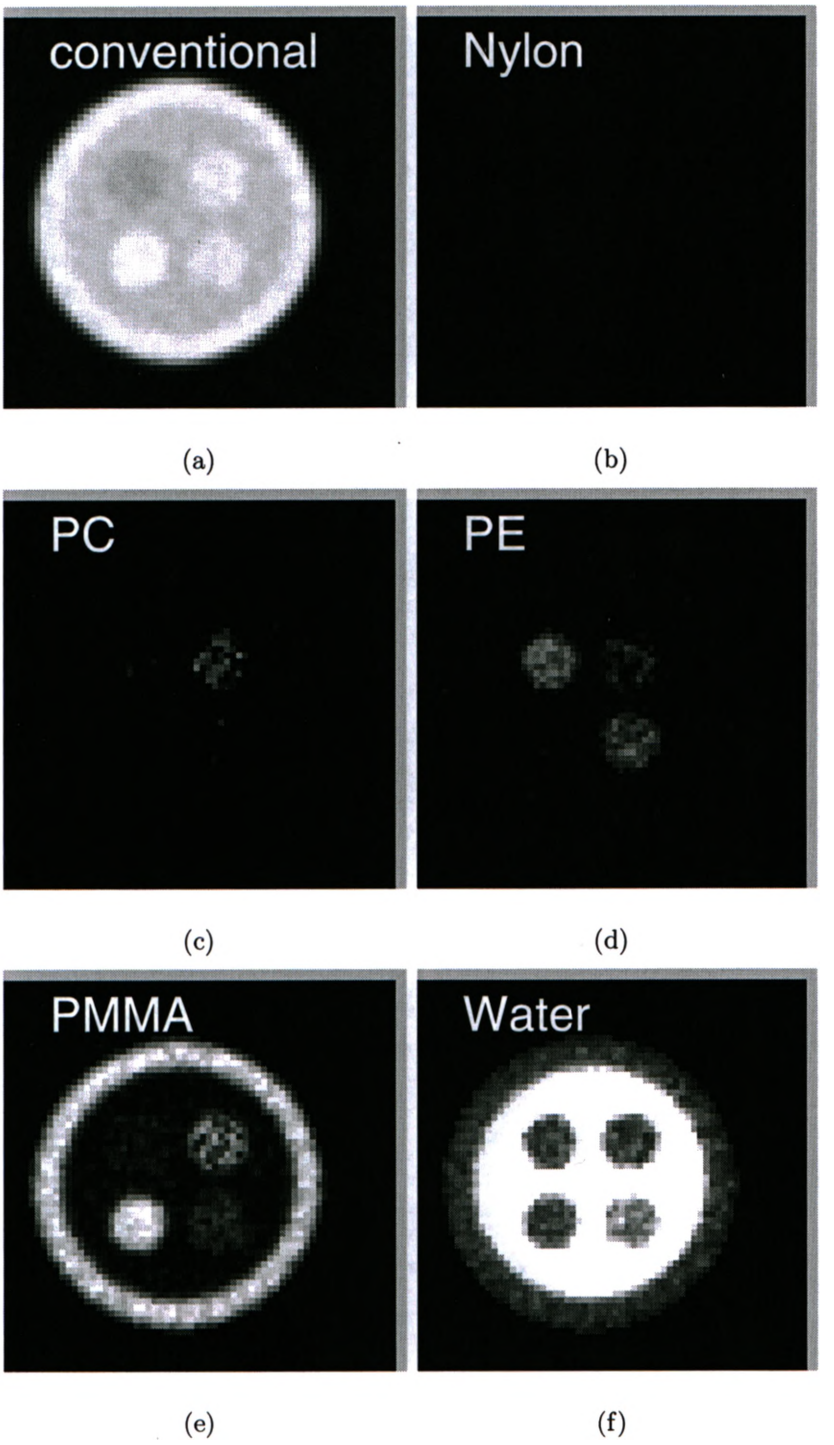

Fig. 3.9: Relative mass-density distribution of the AAPM plastic phantom using a single erbium filter. Due to the increased angular blur due to the increased spectral width, the nylon insert is misidentified as combination of PE, PMMA and water.

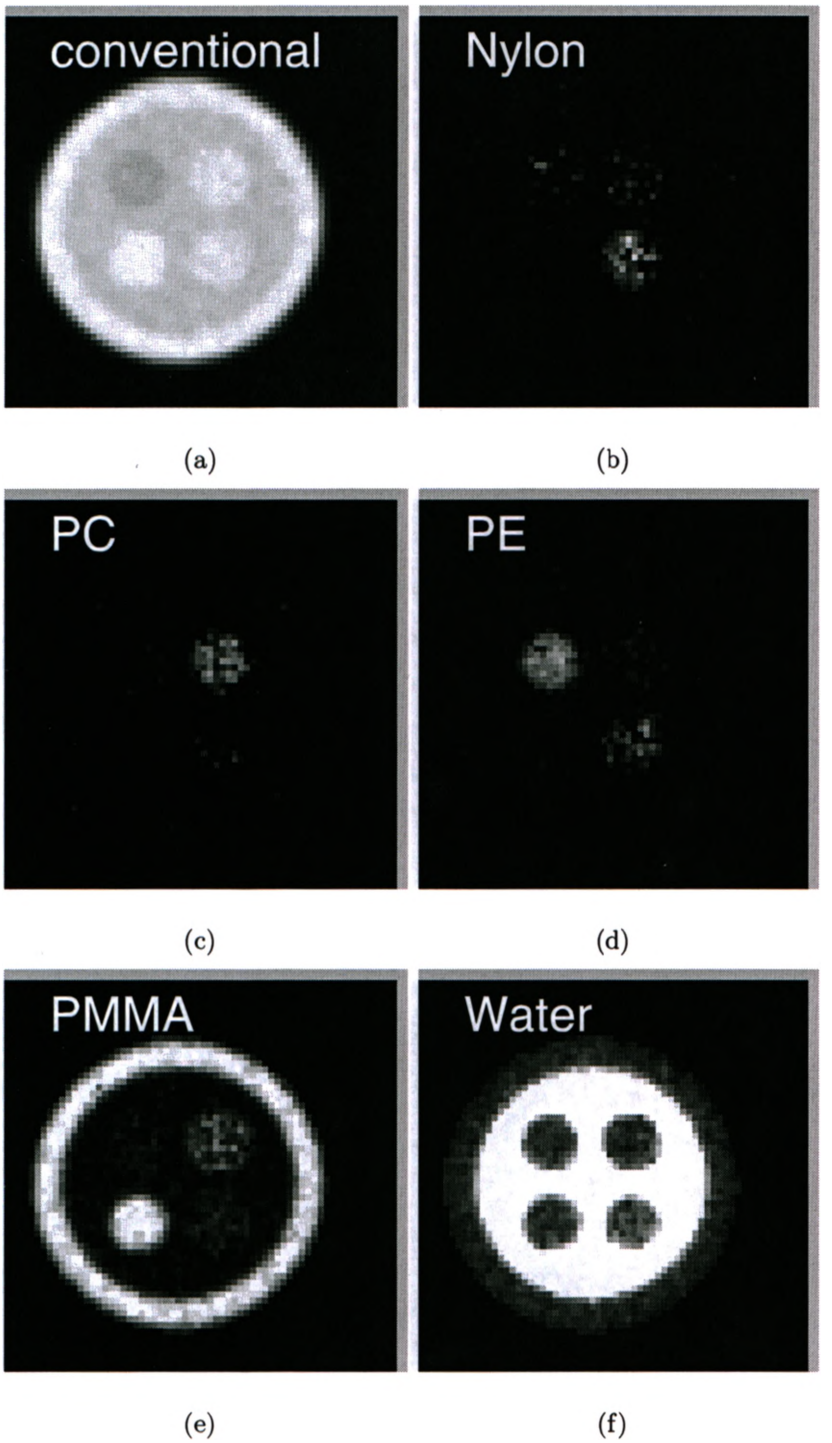

Fig. 3.10: Relative mass-density distribution of the AAPM plastic phantom using a single thulium filter. Material-identification accuracy of the nylon insert is increased compared to the erbium filter. This is most likely due to the decrease in the effective spectral width caused by the strong contribution of tungsten $K_{\alpha 1}$ and $K_{\alpha 2}$ emissions in the thulium-filtered transmission spectrum.

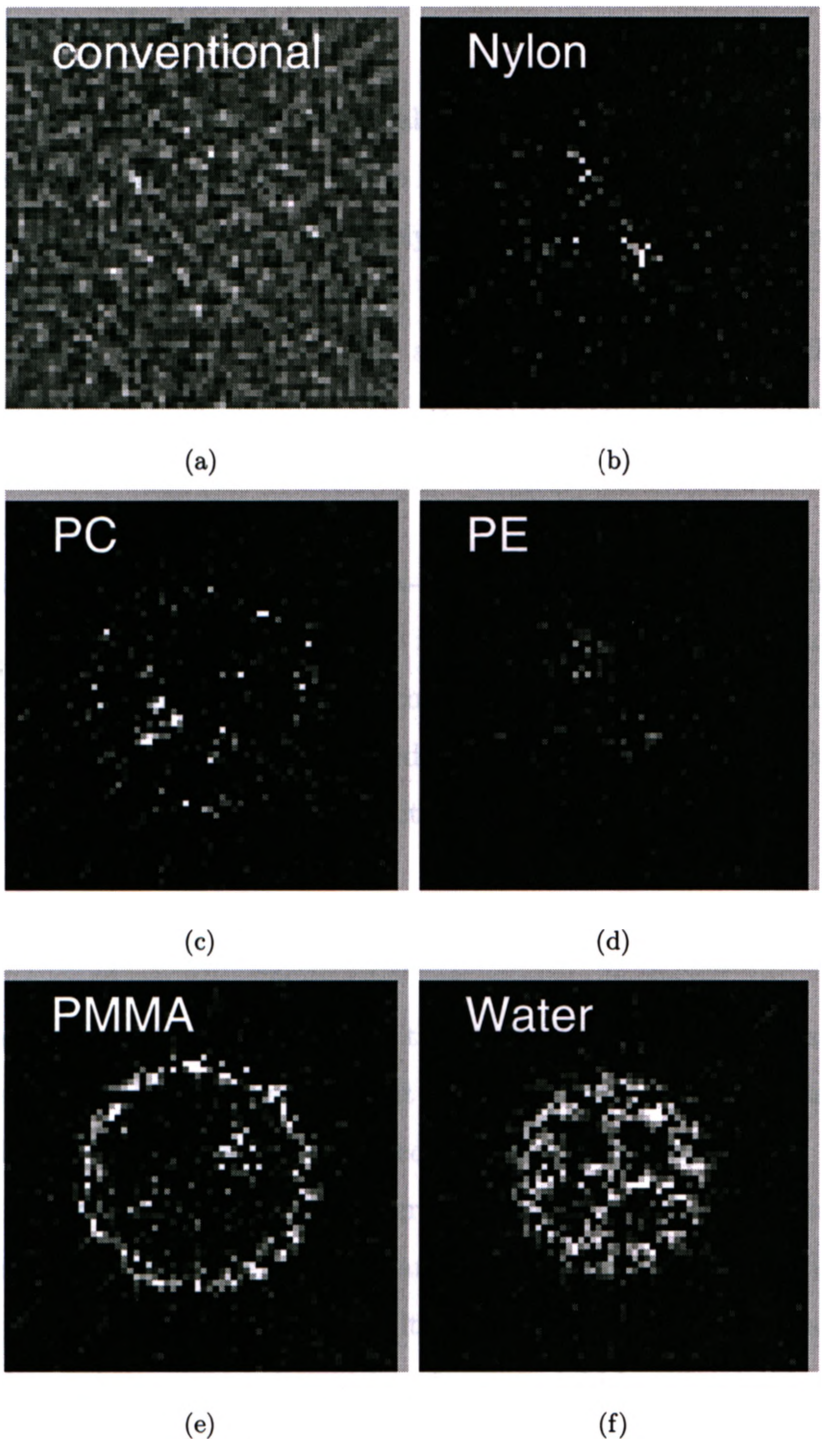

Fig. 3.11: Preliminary relative mass-density distribution of the AAPM plastic phantom using Er-Tm balanced filters. Note that the conventional CT image is particularly noisy because it shows the attenuation differences of the filter passband photons only. These passband photons make up a small percentage of a conventional CT system's spectrum, resulting in a low-contrast, low SNR image.

3.5 Discussion

Balanced-filter CSCT has the potential to be less susceptible to material misidentification than conventional CSCT, due to lower peak overlap in the scatter functions. For example, nylon was almost completely identified as polyethylene in Westmore's material-specific images.[9] This is due to both materials having similar scatter-peak sizes and locations. In theory, the higher angular resolution of balanced-filter CSCT would reduce this misidentification. The low SNR of the balanced-filter mass distribution images obtained here makes it unclear if identification accuracy has improved for the nylon and polyethylene inserts.

Given adequate signal (via increasing x-ray source intensity or scan times), balanced-filter CSCT may have a unique ability to identify materials at a specific locations in a specimen. Conventional CT or CSCT could be used to generate a rough picture of a specimen, which would then be followed by a bulk balanced-filter measurement in a volume-of-interest where material detection is desired.

3.6 Conclusion

It has been shown theoretically that the mass-density distributions of materials in a specimen can be determined without knowledge of the reference sample's mass density or thickness, in coherent-scatter computed tomography.

Balanced-filter coherent scatter tomographic images have been acquired of a medically relevant phantom. The superior angular resolution of balanced-filter CSCT was demonstrated. Compared to single-filter CSCT at a similar tube loading, the observed signal-to-noise ratio was insufficient for material identification in the phantom studied. Balanced-filter CSCT may be effective in identifying the material composition of a specific volume in a specimen, where the improved angular resolution in the measured scatter function would improve material identification accuracy.

References

[1] P. C. Johns and M. J. Yaffe. Coherent scatter in diagnostic radiology. *Med Phys*, 10(1):40–50, 1983.

[2] D. A. Bradley and A. M. Ghose. Photon scattering in biomedically important elements. *Phys Med Biol*, 29(11):1385–1397, Nov 1984.

[3] D. A. Bradley, D. R. Dance, S. H. Evans, and C. H. Jones. Quantitative measurement of small-angle gamma ray scattering from water, nylon, and lucite. *Med Phys*, 16(6):851–857, 1989.

[4] J. Kosanetzky, B. Knoerr, G. Harding, and U. Neitzel. X-ray diffraction measurements of some plastic materials and body tissues. *Med Phys*, 14(4):526–532, 1987.

[5] G Harding, J Kosanetzky, and U Neitzel. Elastic scatter computed tomography. *Phys Med Biol*, 30(2):183–186, 1985.

[6] G. Harding, J. Kosanetzky, and U. Neitzel. X-ray diffraction computed tomography. *Med Phys*, 14(4):515–525, 1987.

[7] G. Harding and B. Schreiber. Coherent x-ray scatter imaging and its applications in biomedical science and industry. *Radiation Physics and Chemistry*, 56:229–245, 1999.

[8] M. S. Westmore, A. Fenster, and I. A. Cunningham. Angular-dependent coherent scatter measured with a diagnostic x-ray image intensifier-based imaging system. *Med Phys*, 23(5):723–733, 1996.

[9] M. S. Westmore, A. Fenster, and I. A. Cunningham. Tomographic imaging of the angular-dependent coherent-scatter cross section. *Med Phys*, 24(1):3–10, 1997.

[10] R. J. Leclair and P. C. Johns. Analysis of spectral blur effects in x-ray scatter imaging. *Med Phys*, 26(9):1811–1816, 1999.

[11] Brian W. King and Paul C. Johns. Measurement of coherent scattering form factors using an image plate. *Phys Med Biol*, 53(21):5977–5990, 2008.

[12] P.A. Ross. Polarization of x-rays. *Phys Rev*, 28:425, 1926.

[13] S. R. Beath and I. A. Cunningham. Pseudo-monoenergetic x-ray diffraction measurements using balanced filters for coherent scatter computed tomography. *Medical Physics*, 36, 2009 (in press).

[14] Deidre L Batchelar, Samuel S Chun, Timothy A Wollin, James K Tan, Darren T Beiko, Ian A Cunningham, and John D Denstedt. Predicting urinary stone composition using x-ray coherent scatter: a novel technique with potential clinical applications. *J Urol*, 168(1):260–265, 2002.

[15] Melanie T. M. Davidson, Deidre L. Batchelar, Sujeevan Velupillai, John D. Denstedt, and Ian A. Cunningham. Analysis of urinary stone components by x-ray coherent scatter: characterizing composition beyond laboratory x-ray diffractometry. *Phys Med Biol*, (16):3773–3786, 2005.

[16] H. E. Johns and J. R. Cunningham. *The physics of radiology.* Charles C. Thomas, Springfield IL, 4th edition, 1983.

[17] P.C. Johns and M.P. Wismayer. Measurement of coherent x-ray scatter form factors for amorphous materials using diffractometers. *Phys Med Biol*, 49(23):5233–5250, 2004.

[18] Jiang Hsieh. *Computed Tomography: Principles, Design, Artifacts, and Recent Advances.* SPIE Publications, 2003.

Chapter 4

Conclusions and future work

This chapter concludes the dissertation. Section 4.1 summarizes the conclusions of this work based on the results of previous chapters. Avenues for future research, which include potential improvements to this work are discussed in Section 4.2.

4.1 Conclusions

The goal of this thesis was to investigate the use of balanced filters to produce pseudo-monoenergetic scatter functions for coherent-scatter imaging. Of particular importance is the choice of filter materials and thickness. Use of filters with a small atomic-number difference (ΔZ) will produce the least angular blur, but also result in a smaller "difference spectrum"[1] and therefore more statistical uncertainty in the measurements. Thus, it is important to choose filters that have the largest acceptable ΔZ value without increasing blur substantially.

The following specific conclusions were made from this work:

1. Geometric factors can play a dominant role in determining the angular blur of measured scatter patterns. In particular, it was determined that focal-spot size and beam width are responsible for limiting RMS angular blur to approximately

0.12° (3% at 6°) under the experimental conditions (1-mm focal spot, 1-mm beam width).

2. A K-edge energy difference of approximately 1.9 keV with a mean energy of 58.4 keV can be achieved using balanced filters (Er and Tm), corresponding to a relative RMS spectral width of approximately 1%.

3. Bragg-peak RMS relative width of approximately 3% at a scatter angle of 6° was observed in Al powder, consistent with a theoretical model of scatter-function blur. It is thought that at higher scatter angles, oblique incidence on the XRII curved input phosphor (causing photon energy to be spread over multiple pixels) and off-axis electron-focussing issues may be responsible for increased blur.

4. It was shown theoretically that coherent-scatter computed tomography can determine mass-density distributions based on base-line scans of reference materials, without knowledge of the materials's mass density or thickness. This allows the use of reference samples having unknown densities, such as small powdered samples.

5. Mass-density distributions of a plastic phantom were obtained using Er-Tm balanced filters. The image signal-to-noise ratio, however, was much lower than that obtained using a single gadolinium filter for the same total tube heat loading. Thus, while the balanced-filter method produces scatter functions with superior angular resolution, substantially longer scan times may be required for high SNR tomographic material maps.

This works supports the following additional conclusions:

1. The source-specimen distance should be as small as possible to maximize scatter intensity, but not less than 25 or 30 cm for a 1-mm focal spot and beam. Blur is reduced gradually with increasing specimen-detector distance.

2. For the conditions in this study, filter atomic number differences of two or three will maximize difference-spectrum intensity with only a minor increase in angular blur.

4.2 Avenues for future research

4.2.1 Bragg-peak NEQ: A new approach to scatter signal and noise using balanced filters

Although this thesis describes the modeling of angular blur in CSCT, the next step in obtaining a complete description of scatter-function measurement performance is examining the tradeoff between angular blur and signal-to-noise ratio. The following is a preliminary suggestion of how this evaluation could be performed. Such a study would be of value when comparing the performance of single-filter vs. balanced-filter CSCT designs.

Theory

Scatter of a monoenergetic beam from a single Bragg plane results in a single peak in C(θ). If N and σ_N represent the mean and standard deviation in the number of quanta scattered by particular Bragg plane (Fig. 4.3), the squared signal-to-noise ratio (SNR) is given by

$$\mathrm{SNR}^2 = \frac{N^2}{\sigma_N^2} = N \tag{4.1}$$

($\sigma_N^2 = N$ since scattered photons are Poisson distributed). This quantity is called the noise-equivalent number of quanta (NEQ) in radiographic imaging[2] and describes the squared SNR that would be obtained using an idea detector (with unity quantum efficiency). In the context of scatter-pattern measurements, we suggest use of the Bragg-peak NEQ as:

$$\mathrm{NEQ}_B = \frac{N^2}{\sigma_N^2} = N, \tag{4.2}$$

describing an equivalent number of Poisson-distributed quanta contributing to the scatter peak. If the mean measurement of peak area in a scatter function is λ and is proportional to the contributing number of scattered photons ($\lambda = kN$ where k is a scaling factor relating N to the measured quantity such as a digital value), then a measurement of the Bragg-peak NEQ is described by

$$\mathrm{NEQ}_B = \frac{\lambda^2}{\sigma^2}. \tag{4.3}$$

A theoretical estimate of NEQ_B when using balanced filters is obtained with reference to Eq. (2.3) integrated over solid angles. The spectrum of photons scattered from a uniform specimen with single-electron linear coherent-scatter coefficient $\mu_{coh} = n_o(E)\sigma_{coh}(E)$, is given by

$$\frac{\mathrm{d}N(E)}{\mathrm{d}E} = \frac{\mathrm{d}N_o(E)}{\mathrm{d}E} W\mu_{coh}(E)e^{-\frac{\mu}{\rho}(E)\rho W}. \tag{4.4}$$

A measurement of λ is given approximately by:

$$\begin{aligned}\lambda \;\approx\; & k\zeta \int_{K_L}^{K_H} \alpha(E) \left(\frac{\mathrm{d}N_H(E)}{\mathrm{d}E} - \frac{\mathrm{d}N_L(E)}{\mathrm{d}E}\right) \\ & \times W\mu_{coh}(E)e^{-\frac{\mu}{\rho}(E)\rho W}\,\mathrm{d}E,\end{aligned} \tag{4.5}$$

where K_L and K_H are the K-edge energies of the low and high-Z filters respectively and ζ is the fraction of scattered photons corresponding to the desired Bragg peak. This result depends on the scattering specimen (thickness W, linear interaction coefficient $\mu(E)$, and linear coherent-scatter coefficient $\mu_{coh}(E)$), the source x-ray spectrum $\frac{\mathrm{d}N_o}{\mathrm{d}E}(E)$, filter materials and thicknesses, and the detector quantum efficiency $\alpha(E)$.

Photons also contribute to a scatter peak by satisfying the Bragg relationship at the same angle but other energies, resulting in a variance in λ given by:

$$\begin{aligned}\sigma^2 \;\approx\; & k^2\zeta \int_0^{kV} \alpha(E) \left(\frac{\mathrm{d}N_H(E)}{\mathrm{d}E} + \frac{\mathrm{d}N_L(E)}{\mathrm{d}E}\right) \\ & \times W\mu_{coh}(E)e^{-\frac{\mu}{\rho}(E)\rho W}\,\mathrm{d}E.\end{aligned} \tag{4.6}$$

As an alternative to the Bol-Saito criterion,[3, 4] we use both N/H and NEQ_B/H as figures of merit for maximizing scatter-function SNR where $H = kV \times mAs \times 1.35$

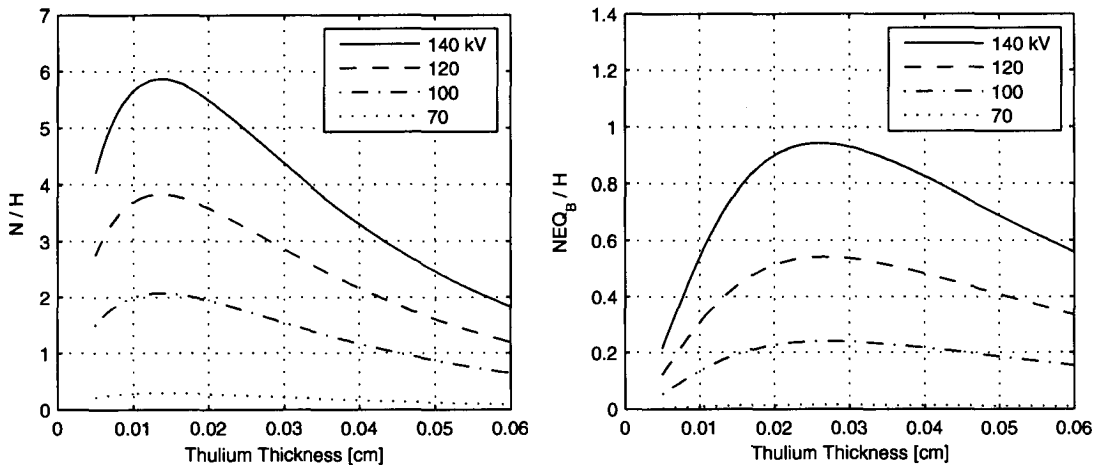

(a) (b)

Fig. 4.1: Theoretical calculation of the two figures of merit for imaging calcium oxalate as a function of filter thickness for a balanced Er-Tm pair: (a) number of detected coherent-scatter passband photons per unit tube heat load, N/H, using Eq. (2.22); and (b) Bragg-peak NEQ per unit heat load, NEQ_B/H.

is the tube heat load in "heat units" and is proportional to the heat energy deposited in the tube anode (Fig. 4.1).

Optimal parameters for x-ray diffraction measurements are task dependent. A majority of kidney stones consist of calcium oxalate with a density of approximately 2 g/cm^3,[5] and most calculi have diameters less than 1 cm when removed by percutaneous nephrolithotripsy or ureteroscopy. Figure 4.1 shows curves of N/H and NEQ_B/H with $\zeta = 1$ and $W = 1$ cm as a function of filter thickness for balanced Er-Tm filters and a range of kV values. Detector quantum efficiency was approximated as the interaction probability in 0.4 mm of CsI. The N/H curves increase with kV and, as expected, have maxima at filter thickness given by the Bol-Saito criterion that are independent of kV. The NEQ_B/H curves have broad maxima indicating that optimal results can be achieved with filter thicknesses anywhere in the range 0.015 to 0.04 cm. Specimen thickness did not alter these optimal thicknesses for all values tested ($W = 0.1$ to 1.0 cm). Since use of thinner filters results in a larger number of

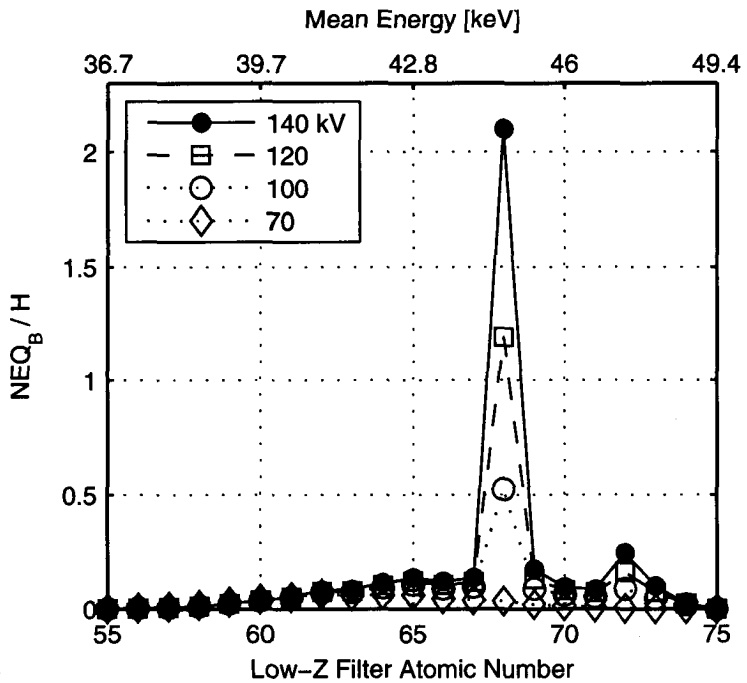

Fig. 4.2: Scatter-peak NEQ per unit tube heat load for various combinations of filters whose atomic numbers differ by 1 ($W = 1$ cm, $\rho = 2$ g/cm^3 of Ca, Bol-Saito filter thicknesses).

detected photons and the Bol-Saito criterion was consistent with the thin-filter end of the NEQ_B/H optimum, Bol-Saito thicknesses were used in all experimental tests.

The effective energy of the difference spectrum is determined by the average filter atomic number as illustrated in Fig. 4.2, showing theoretical values of NEQ_B/H for balanced filters with atomic numbers between 55 and 75, using a range of kV values. The maximum NEQ_B/H value is obtained using Er-Tm filters as they isolate the tungsten K-alpha doublet ($\approx$ 58 kV) at higher tube voltages (eg. 140 kV). Both are readily available as metal foils from commercial suppliers. Table 2.1 lists other potential filter combinations.

Preliminary Results

The area of peak A in (Fig. 2.7) had mean $\lambda_A = 0.46$ (relative units) and standard deviation $\sigma_A = 0.008$ as determined by fitting Gaussian curves to each of seven independent trials. Both of these values are proportional to the number of interacting photons, giving

$$\mathrm{NEQ}_A = \frac{\lambda_A^2}{\sigma_A^2} = 3.3 \times 10^3 \tag{4.7}$$

using equation Eq. (4.2). The expected upper and lower 90% confidence limits in the precision measurement σ_A are approximately +80% and -30% (short-term precision in 7 repeated measurements assuming a normal distribution[6]) corresponding to a 90% confidence range in measurements of NEQ_A as $1.3 \times 10^3 \leq \mathrm{NEQ}_A \leq 5 \times 10^3$.

A theoretical estimate was obtained for these conditions using Eqs. (4.2) - (4.6) with $\zeta_A = 0.148$ (see Appendix 4.A), resulting in

$$\mathrm{NEQ}_A = \frac{N_A^2}{\sigma_A^2} = 3.1 \times 10^3. \tag{4.8}$$

X-ray quanta are Poisson distributed and hence the uncertainty in this calculation is approximate, but the excellent agreement gives confidence that we have a reasonable method of predicting noise in scatter functions obtained using balanced filters.

Preliminary Conclusion

Maximizing both the number of scatter photons per unit tube heat load in the Bragg peaks (Fig. 4.1a), and Bragg-peak NEQ per unit heat load (Fig. 4.1b), requires the largest acceptable kV value with filter thicknesses approximately equal to the Bol-Saito optimal thickness. Further study is needed to validate the Bragg-peak NEQ for different filter combinations ($\Delta Z > 1$) as well as for comparison to the conventional single-filter CSCT used in previous studies.

4.2.2 In situ stone analysis using a log-spiral crystal

It has been demonstrated that coherent-scatter analysis can provide kidney-stone composition information; information that physicians could use to choose the most effective treatment plan. The challenge is to scale the CSCT system from being limited to small specimens (< 3 cm in size) to being able to accommodate an entire human torso.

The development of log-spiral crystal technology operating in the transmission (Laue) geometry has been shown to effectively diffract x rays of a specific wavelength that originate from a point source.[7] For the task of imaging a kidney stone within a human body, a tiny pencil-beam of x rays would illuminate the stone located by a prior stereotactic radiography procedure. Photons in the incident beam undergo coherent scatter in the stone (as well as elsewhere along the incident beam path) and these scattered photons would travel at small angles out of the body. It is known that log-spiral crystals have scatter acceptance angles that could easily accommodate the range of angles involved in coherent scattering at photon energies sufficient for *in situ* imaging (40-100 keV, < 10°). Thus if such a crystal were to be placed immediately beyond the body, in the path of the stone-scattered photons, it may be possible to detect these diffracted photons and extract useable scatter functions from them.

Log-spiral crystals are known to have diffraction efficiencies at or above 20% and have been used to develop monochromatic imaging beams from x-ray tube point sources.[8] These efficiencies make possible the use of a conventional x-ray tube as the photon source.

There are a number of things that need to be considered in developing this device. One is non-stone scatter rejection. Scatter from tissues before and aft of the stone will reach the crystal and be diffracted onto the detector surface. The magnitude of this scatter compared to scatter coming from the stone will have to be determined to ensure there is enough signal-to-noise ratio to do a meaningful material analysis. Secondly, unlike laboratory kidney stone analysis where dose is not an issue, there

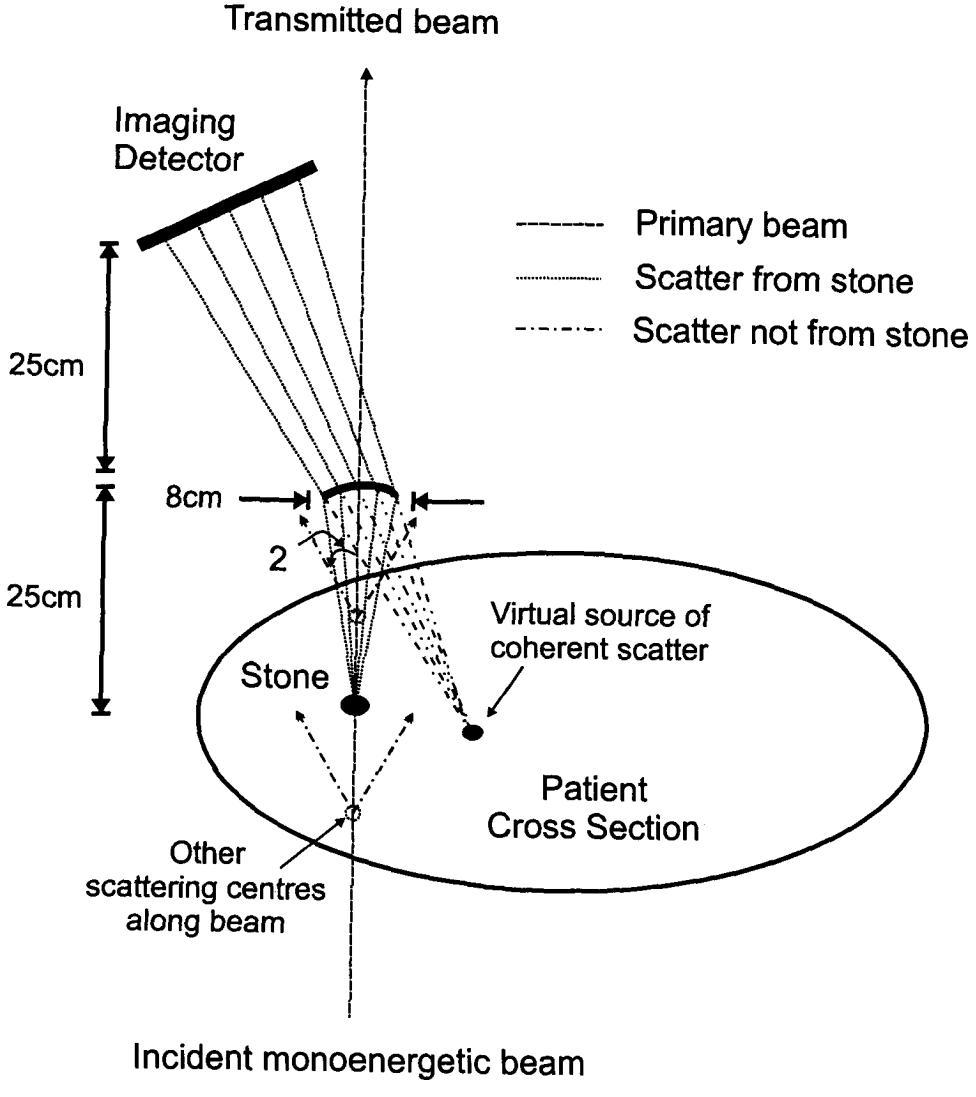

Fig. 4.3: Illustration of the log-spiral Laue crystal used to select coherent-scatter coming from a stone *in situ*. The reflection angle directing the beam towards the imaging detector is exaggerated for the illustration.

may be difficulties obtaining meaningful scatter-function signal while maintaining human-acceptable levels of dose.

A narrow wavelength x-ray source would limit non-stone scatter accepted by the log-spiral crystal, thus a monoenergetic x-ray source may be favored for this application. It is unlikely balanced filters would be acceptable in those role, however, as two exposures are required, potentially increasing dose and increasing the likelihood that the patient may have shifted position between exposures.

If these challenges are met this would be the only method able to determine stone composition in situ.

4.2.3 Energy-discriminating imaging

The development of photon-counting and energy-discriminating flat-panel detectors may hold incredible potential for coherent-scatter imaging. Use of photon-counting detectors results in scatter images with no additive (such as electronic) detector noise, as they are sensitive enough to detect single photon interactions as opposed to producing a signal proportional to the energy transferred by interacting photons. Energy-discriminating detectors incorporate a pulse-height analysis of each detection event, and a spectrum of interaction energies is recorded for each detector element. This is attractive because once the energy and scatter angle of each x ray is determined, the scatter angle can be numerically altered to correspond to a different x-ray energy. In this way, a monoenergetic scatter function could be obtained using a wide spectrum of x-ray energies without the need for filters or monochromators. This would allow the use of low-power x-ray generators and tubes. This approach will be degraded by interactions that do not deposit all of the x-ray energy in a single detector element. Photoelectric or Compton interactions may produce a scatter photon that will reduce the absorbed energy and could be confused with a photon having less energy.

Recently, a number of technologies have been introduced that offer intriguing en-

ergy resolution capabilities, while not sacrificing the spatial resolution capabilities of current intensifier/camera and flat-panel detector systems.[9] For example, Limousin describes a CdZnTe detector with a 600 μm pixels size (twice the pixel size used in this study, but tolerable for CS imaging) and a FWHM energy resolution of 1.3% at 60 keV.[10] Shikhaliev predicts SNR improvements up to 42% in projection radiographs of a calcium carbonate contrast element inserted in soft tissue.[11] It is important to note that these applications looked at the improvements to conventional attenuation based radiography. In coherent-scatter imaging, one would expect a more drastic improvement in the scatter-peak NEQ because the large majority of photons coherently scattered from a polyenergetic beam would contribute to scatter-function peaks. At the same time, this would also reduce the number of photons that would be considered background noise. Also, in some biological structures scatter functions may be more orthogonal than material attenuation coefficients (e.g. soft tissue) allowing modalities like CSCT to have superior contrast than attenuation based CT scanners.

A photon-counting energy discriminating detector would also be dose efficient, allowing every photon that undergoes a coherent scatter interaction, no matter what its energy, to provide direct information about the material-specific scatter function.

A known limitation of energy-discriminating detectors is their low count rate. Scatter imaging is a good fit for these detectors because of the lower fluences involved compared to attenuation measurements of the primary beam, such as in CT or conventional radiography.

An energy-discriminating CSCT system may open the door for a host of tissue identification applications considered too dose inefficient for current generation CSCT. For example, CSCT could be used as a non-invasive alternative to biopsy of suspicious breast-lesions for the early detection of breast cancer.[12]

References

[1] S. R. Beath and I. A. Cunningham. Pseudo-monoenergetic x-ray diffraction measurements using balanced filters for coherent scatter computed tomography. *Medical Physics*, 36, 2009 (in press).

[2] R. Shaw. The equivalent quantum efficiency of the photographic process. *J Photograh Sci*, 11:199–204, 1963.

[3] W Bol. The use of balanced filters in x-ray diffraction. *J Sci Instrum*, 44(9):736–739, 1967.

[4] Masatoshi Saito. Quasimonochromatic x-ray computed tomography by the balanced filter method using a conventional x-ray source. *Med Phys*, 31(12):3436–3443, Dec 2004.

[5] R. Munver, P. Zhong, J. Jacobs, A. Hesse, S.C. Muller, and G.M. Preminger. Acoustic and mechanical properties of artificial stones in comparison to natural kidney stones. *J Urol*, 164(2):537–544, 2000.

[6] C.C. Gluer, G.Blake, Y.Lu, B.A.Blunt, M.Jergas, and H.K.Genant. Accurate assessment of precision errors: how to measure the reproducibilty of bone densitometry techniques. *Osteoporosis International*, 5:262–270, 1995.

[7] A. J. Kropf, R. J. Finch, J. A. Fortner, S. Aase, C. Karanfil, C. U. Segre, J. Terry, G. Bunker, and L. D. Chapman. Bent silicon crystal in the laue geometry to resolve x-ray fluorescence for x-ray absorption spectroscopy. *Review of Scientific Instruments*, 74(11):4696–4702, 2003.

[8] Zhong Z., Chapman D., Thomlinson W., Arfelli F., and Menk R. A bent laue crystal monochromator for monochromatic radiography with an area beam.

Nuclear Instruments and Methods in Physics Research Section A: Accelerators, Spectrometers, Detectors and Associated Equipment, 399:489–498(10), 11 November 1997.

[9] Ge Wang, Hengyong Yu, and Bruno De Man. An outlook on x-ray ct research and development. *Medical Physics*, 35(3):1051–1064, 2008.

[10] O. Limousin. New trends in cdte and cdznte detectors for x- and gamma-ray applications. *Nuclear Instruments and Methods in Physics Research Section A: Accelerators, Spectrometers, Detectors and Associated Equipment*, 504(1-3):24–37, 2003.

[11] Polad M Shikhaliev. Tilted angle czt detector for photon counting/energy weighting x-ray and ct imaging. *Phys Med Biol*, 51(17):4267–4287, Sep 2006.

[12] G. Kidane, R. D. Speller, G. J. Royle, and A. M. Hanby. X-ray scatter signatures for normal and neoplastic breast tissues. *Phys Med Biol*, 44(7):1791–802, Jul 1999.

4.A Calculation of ζ_A for aluminum powder

The Bragg-peak NEQ depends on the value of ζ, the fraction of scattered photons that contribute to the peak. For aluminum powder (face-centered cubic, Fm-3m (225), $a = 4.0497$ Å)[1] at 58.4 keV, the number of photons in each peak is proportional to a structure factor, multiplicity factor, and the Lorentz-polarization factor (temperature effects are neglected). The first two are determined by a theoretical calculation resulting in p_j for peak j (Crystal Impact Inc., www.crystalimpact.de). The Lorentz-polarization factor is given by[1]

$$L(\theta) = \frac{(1 + \cos^2\theta)}{\sin^2(\theta/2)\,\cos(\theta/2)} \tag{4.9}$$

where θ is twice the Bragg angle. In powdered polycrystaline materials such as Al, the product $p_j L(\theta_j)$ gives the number of scattered photons per unit length of the jth scatter ring. Thus, $p_j L(\theta_j)\sin(\theta_j/2)$ is proportional to the total scatter in the jth peak,[1] and ζ_A, the lowest-angle peak in Al, is given by:

$$\zeta_A = \frac{p_A L(\theta_A)\sin(\theta_A/2)}{\sum_j p_j L(\theta_j)\sin(\theta_j/2)}. \tag{4.10}$$

Consideration of the first 35 peaks gives $\zeta_A = 0.148$.

References

[1] B.D. Cullity. *Elements of X-ray Diffraction.* Addison-Wesley, 1956.

Appendix A

Permission to reproduce published work

A.1 Permission to use images from the National Kidney and Urological Diseases Information Clearing House (Chapter 1)

---

from NKUDIC

to Stephen Beath

date Tue, Mar 17, 2009 at 2:56 PM

subject RE: Permission to use Image

Thank you for contacting the National Kidney and Urologic Diseases Information Clearinghouse (NKUDIC).

Our information including illustrations is not copyrighted. The clearinghouse encourages users of our e-publications to duplicate and distribute as many copies as desired.

Also, you may use NIDDK Image Library to find illustrations for your thesis presentation. The NIDDK Image Library is a searchable database of original full-color and black-and-white illustrations produced by the NIDDK Information Clearinghouses that are available copyright free to the public at no cost. To access the Image Library, please see: www.catalog.niddk.nih.gov/ImageLibrary/

We do ask that you credit each illustration downloaded as follows: National Institute of Diabetes and Digestive and Kidney Diseases, National Institutes of Health.

Unfortunately, orders may be mailed only to locations in the United States and U.S territories. However, feel free to visit our website and reproduce copies of our publications from there.

Most of our publications may also be found online and are listed at the following website address: www.kidney.niddk.nih.gov/kudiseases/a-z.asp.

We hope that you find this information helpful.

NKUDIC 3 Information Way Bethesda, MD 20892-3580 Phone: 1-800-891-5390 Fax: 703-738-4929 Email: nkudic@info.niddk.nih.gov Internet: www.kidney.niddk.nih.gov or www.urologic.niddk.nih.gov

—Original Message—

From: Stephen Beath

Sent: Monday, March 16, 2009 2:17 AM

To: NKUDIC

Subject: Permission to use Image

Hello,

I am a M.Sc. candidate at the University of Western Ontario (London, Ontario, Canada), doing a degree related to kidney stone disease. I hoped to use an image from your site to include in my thesis introduction (not for peer-reviewed publication.) This image is:

Waste.gif

from this page:

kidney.niddk.nih.gov kudiseases pubs stones ez index.htm

in the "What do my kidneys do?" section.

I hope to get confirmation from you that this is permissible? If you require more information from me, please let me know.

Thank you for your time,

Sincerely,

Stephen Beath

A.2 Permission to reproduce article accepted in Medical Physics (Chapter 2)

---

from JOURNAL

to Stephen Beath

date Mon, Mar 16, 2009 at 8:55 AM

subject Re: Permission to include publication in M.Sc. thesis

Hi Stephen,

Yes, you may have permission to reprint your recently accepted manuscript for your dissertation. Please let me know if you need anything else.

Thanks,

Penny Slattery Journal Manager

¿¿¿ Stephen Beath 3/16/2009 2:05 AM ¿¿¿

To whom it may concern,

I am completing a masters dissertation at the University of Western Ontario, London, Ontario, Canada, entitled "Pseudo-monoenergetic x-ray diffraction measurements using balanced filters for coherent-scatter computed tomography". I would like your permission to reprint in my thesis the paper recently accepted for publication in the Medical Physics journal with the same title (Ref: MS 08-406)

Thank you for your consideration of this request. Sincerely,

Stephen Beath